Computers & Fluids 103 (2014) 290–306

Contents lists available at ScienceDirect

Computers & Fluids

journal homepage: www.elsevier.com/locate/compfluid

Numerical investigation of chemotaxic phenomenon in incompressible viscous fluid flow

Tony W.H. Sheu [a,b,c,*], Chen Yu Chiang [a]

[a] Department of Engineering Science and Ocean Engineering, National Taiwan University, Taipei, Taiwan
[b] Institute of Applied Mathematical Sciences, National Taiwan University, Taipei, Taiwan
[c] Center of Advanced Study in Theoretical Sciences (CASTS), National Taiwan University, Taipei, Taiwan

ARTICLE INFO

Article history:
Received 3 April 2013
Received in revised form 29 May 2014
Accepted 21 July 2014
Available online 4 August 2014

Keywords:
Chemotaxis
Incompressible viscous fluid flow
Blow-up
Combined compact difference scheme
Keller-Segel equations
Coupled KS–NS

ABSTRACT

This study aims to get some details of the chemotaxic phenomena in a domain containing an incompressible viscous fluid by the proposed numerical method. We are also aimed to numerically revisit the classical blow-up phenomenon regarding the initially prescribed cell density in an infinitely larger domain. To get a computationally more accurate scheme for solving the Keller-Segel (KS) [1] equations with/without coupling with the nonlinear hydrodynamic equations, a combined compact difference scheme of fifth-order spatial accuracy is developed in a three-point grid stencil. Three different sets of Keller-Segel equations, which are all amenable to exact solutions with/without coupling with the incompressible Navier–Stokes (NS) equations, are solved to numerically verify the proposed combined compact difference scheme and the incompressible flow solver. How the cell density and chemical concentration are affected by flow convection and diffusion effects will be investigated by solving the coupled KS–NS differential equations.

1. Introduction

Chemotaxis is a biological process observed quite often in various chemical-containing environments, within which somatic cells, bacteria, and many other single/ multiple organisms coexist [8]. This cellular function appears also in life cycle of animals during cancer metastasis. As chemical gradient is non-negligibly small, bacteria may chemotax through the methyl-accepting chemotaxis proteins (MCPs). These transmembrane receptors can bind either with attractants or repellents through a complex protein interaction. Signals released from these receptors can transmit into the cytosol across the plasma membrane.

The direct consequence of chemotaxic event is the generation of an overall movement or an orientation of the organism (or cell) along the chemical concentration gradient [2]. This distinguished cell movement has been known to occur along the direction toward or away from the chemical stimulus. Positive chemotaxis corresponds to cell movement toward a higher concentration of the chemical in question. Conversely, negative chemotaxis has association with cell movement along opposite direction. This concentration-driven movement is important for the survival of bacteria [3]. While a bacterium senses a concentration gradient in its living environment, it will move in correct direction. The nature of bacteria moving toward an attractant, glucose for example, and away from a repellent, phenol for example, plays an essential role of determining whether its life will get better or become worse on the contrary.

The rest of this paper is organized as follows. The Keller-Segel (KS) equations, which are coupled with the incompressible hydrodynamic equations, are presented in Section 2. In Section 3, the combined compact difference scheme (CCD) developed in a stencil of three grid points is proposed to solve the equations cast in a convection–diffusion-reaction form. Incompressible flow solver developed for a viscous fluid is also briefly described in this section. To verify the proposed high-order accurate combined compact difference scheme and the divergence-free compensated solution algorithm, three sets of equations containing the Keller-Segel equations amenable to exact solutions are solved in Section 4. In Section 5, the numerically verified finite difference code is applied to study first the blow-up phenomenon in KS equations [4,5]. The physical details of chemotaxis in the investigated incompressible fluid flow is then enlightened. Finally, we draw some conclusions in Section 6.

* Corresponding author at: Institute of Applied Mathematical Sciences, National Taiwan University, Taipei, Taiwan. Tel.: +886 2 33665746; fax: +886 2 23929885.
E-mail address: twhsheu@ntu.edu.tw (T.W.H. Sheu).

http://dx.doi.org/10.1016/j.compfluid.2014.07.023
0045-7930/

Table 1
Coefficients shown in the working Eqs. (6)–(8).

Equations	ϕ	a	b	c	k	f
(6)	u'	u'	v'	0	Sc	$-Sc\nabla P' - \gamma Scn' - \frac{\partial u'}{\partial t}$
(7)	n'	u'	v'	0	1	$\alpha\nabla\cdot[r(c')n'\nabla c'] - \frac{\partial n'}{\partial t}$
(8)	c'	u'	v'	0	δ	$-\beta r(c')n' - \frac{\partial c'}{\partial t}$

2. Mathematical model

In this study we aim to study the time evolving motile cell, bacterium for example, motion in a flow domain containing oxygen. To model the chemotaxis-driven flow motion generated by oxygen-sensitive bacteria, many mathematical biology models have been developed in the literature since 1970. These model developments are related to many biological applications regarding the proliferation of bacteria, tumor growth/angiogenesis/haptotaxis, and immunology for the production of chemokines near infection sites. The insemination of breeding concern for sea urchins is another representative example. Depending on the biological complexity, chemotaxis can exhibit nonlinear behavior due to the indispensable kinetics in the transport equation for cell

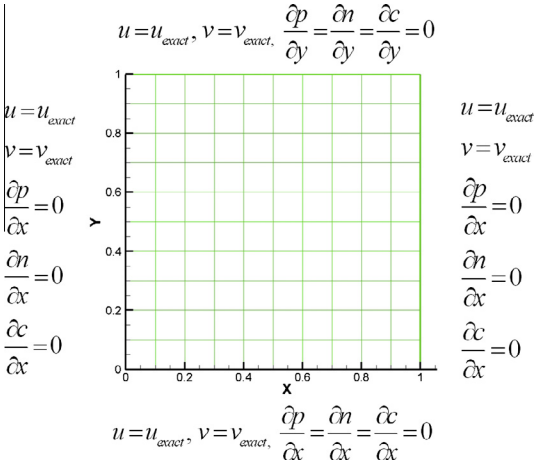

Fig. 3. Illustration of the specified boundary conditions for u, v, p, n and c.

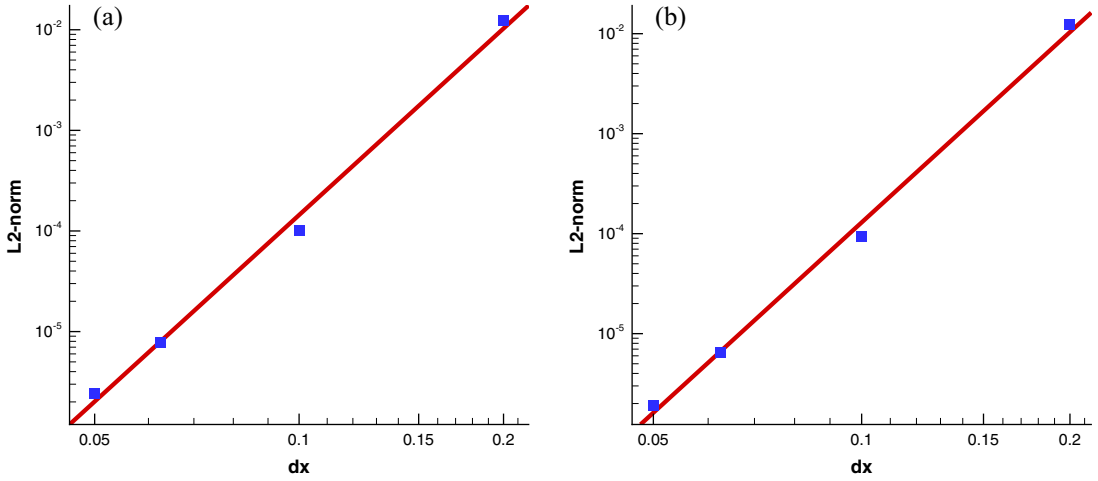

Fig. 1. The computed rates of convergence (roc) for n and c governed by the original Keller-Segel equations investigated in Section 4.1. (a) roc = 6.15915 for n; and (b) roc = 6.32325 for c.

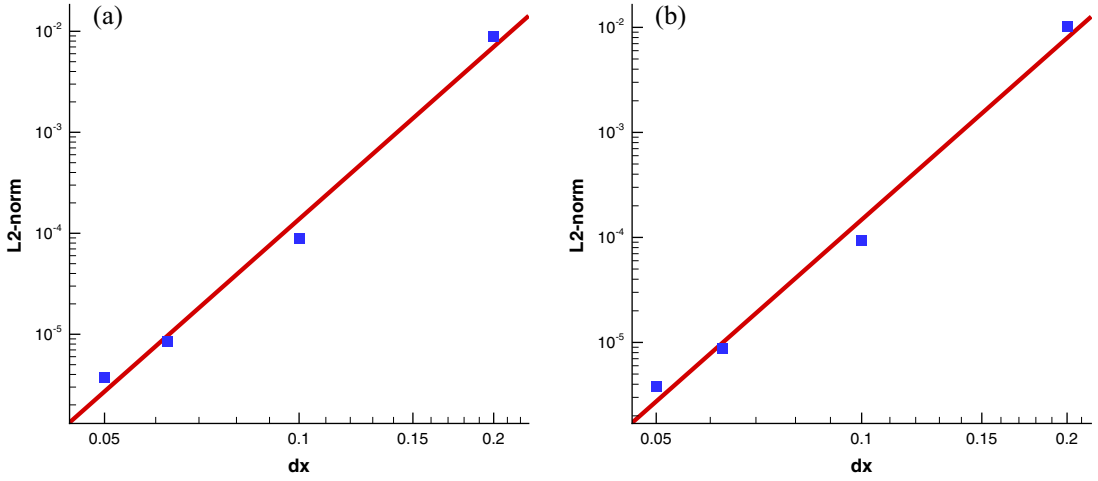

Fig. 2. The computed rates of convergence (roc) for n and c governed by the elliptic–parabolic Keller-Segel equations investigated in Section 4.2. (a) roc = 5.74771 for n; and (b) roc = 5.66896 for c.

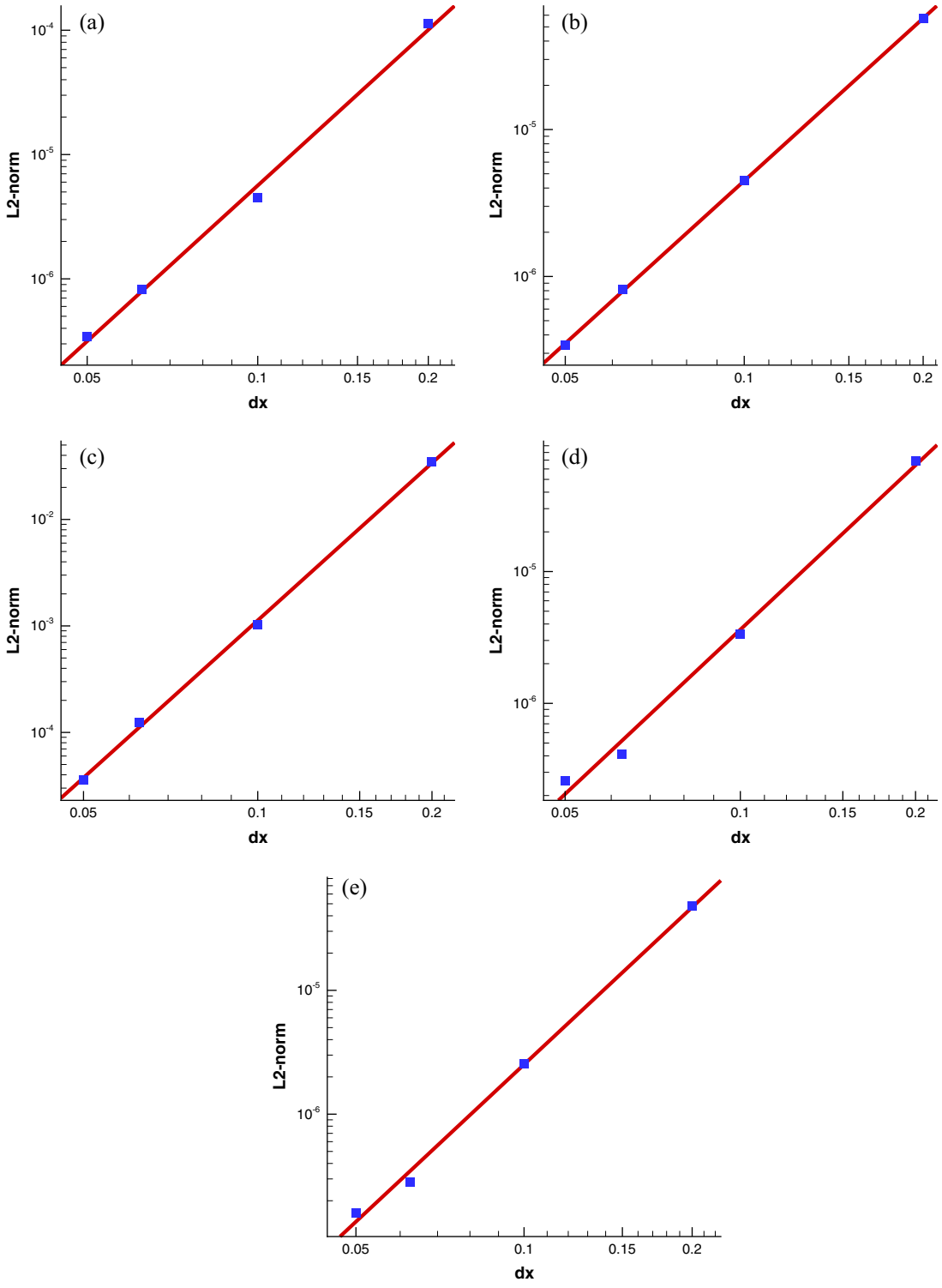

Fig. 4. The computed rates of convergence (roc) for the coupled set of Navier–Stokes and Keller-Segel equations. (a) roc = 4.16056 for u; (b) roc = 3.67536 for v; (c) roc = 4.90904 for p; (d) roc = 4.14300 for n; and (e) roc = 4.21698 for c.

density. Biological complexity can be also resulted from the functional dependence of chemotaxis coefficient on the cell density itself and on the chemical concentration.

In this study, the biological model is considered without taking the logistic event into account. The resulting set of the equations given below is adopted for governing the transport of bacterium cell density (or concentration) n [ML^{-3}] and the time evolving concentration of oxygen c[ML^{-3}]:

$$\frac{\partial n}{\partial t} + \underline{u} \cdot \nabla n = D_n \nabla^2 n - \nabla \cdot \underline{J}, \tag{1}$$

$$\frac{\partial c}{\partial t} + \underline{u} \cdot \nabla c = D_c \nabla^2 c + nf(c) - c\kappa. \tag{2}$$

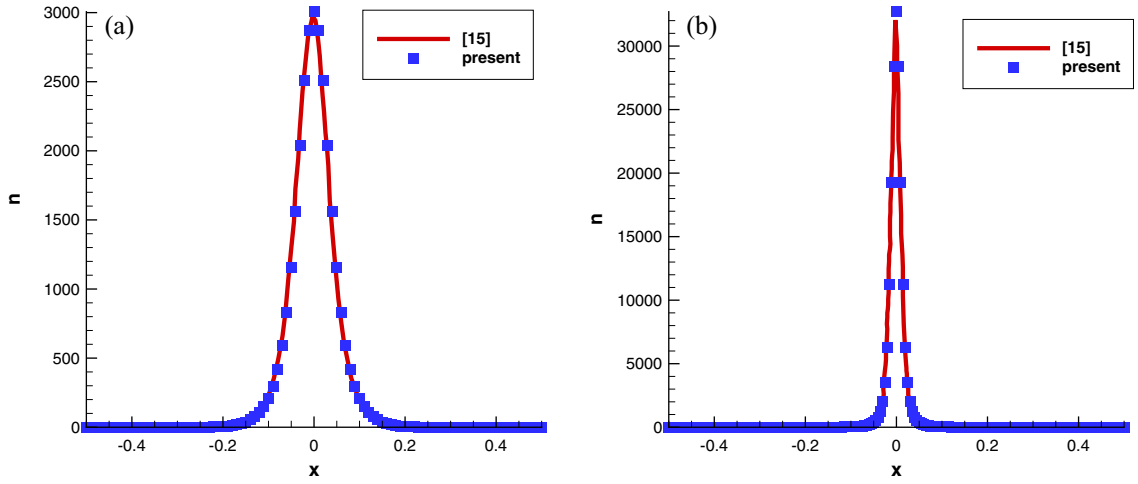

Fig. 5. Comparison of the predicted and referenced solutions along the line $y = 0$ for the values of n computed at two different times and meshes. (a) $t = 5 \times 10^{-6}$; and (b) $t = 2 \times 10^{-5}$.

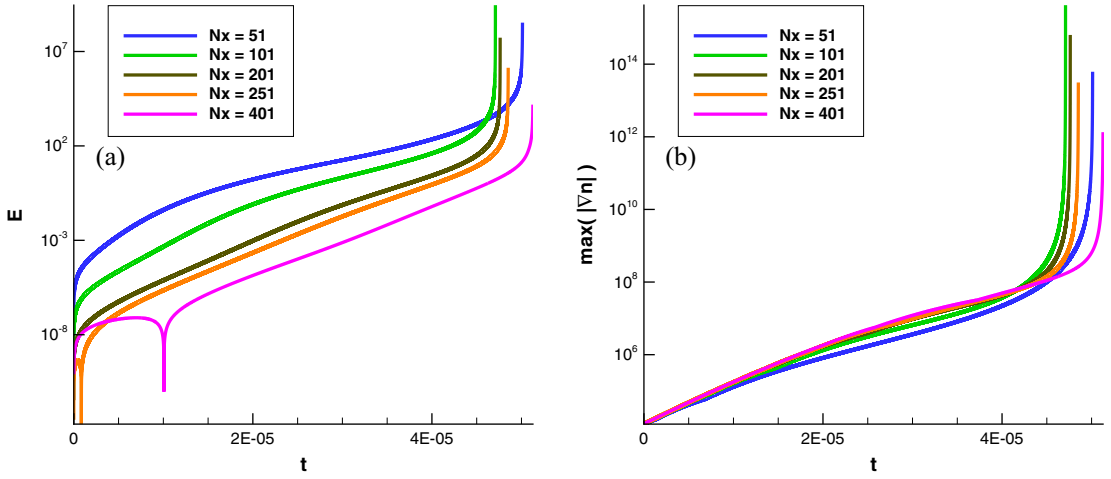

Fig. 6. (a) The predicted total mass difference $E = \int\int n_0 dx\, dy - \int n(x, y, t) dx\, dy$ with respect to time; (b) the predicted maximum value of ∇n along the line $x = 0$ versus time.

Table 2
The blowup times predicted at different grid spacings Δx.

dx	0.02	0.01	0.005	0.004	0.0025
Total mass	6.614×10^{9}	3.633×10^{7}	3.100×10^{8}	1.019×10^{8}	5.867×10^{8}
Blowup time	5.362×10^{-5}	5.034×10^{-5}	5.101×10^{-5}	5.179×10^{-5}	5.399×10^{-5}

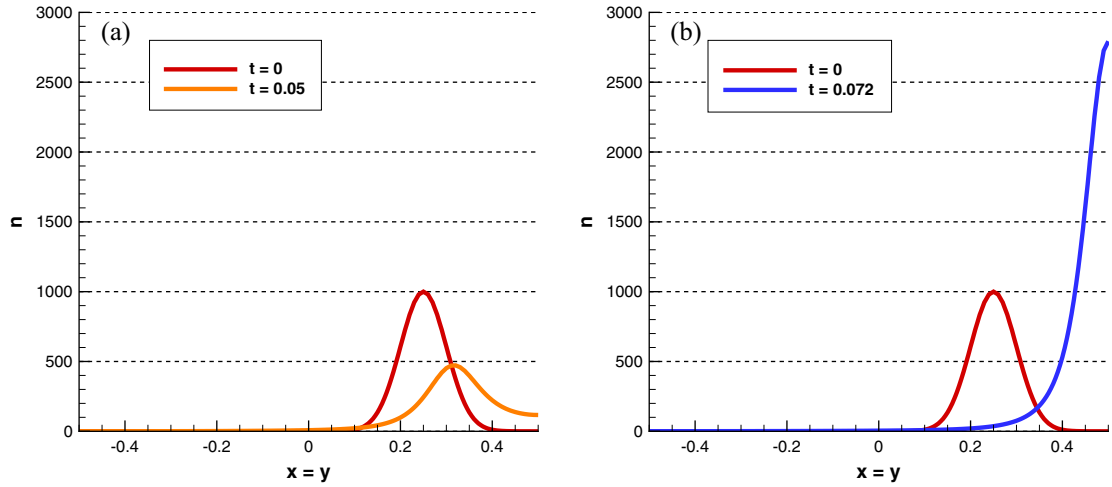

Fig. 7. The predicted profiles of n along the line $x - y = 0$. (a) at $t = 0.05$; and (b) at $t = 0.072$.

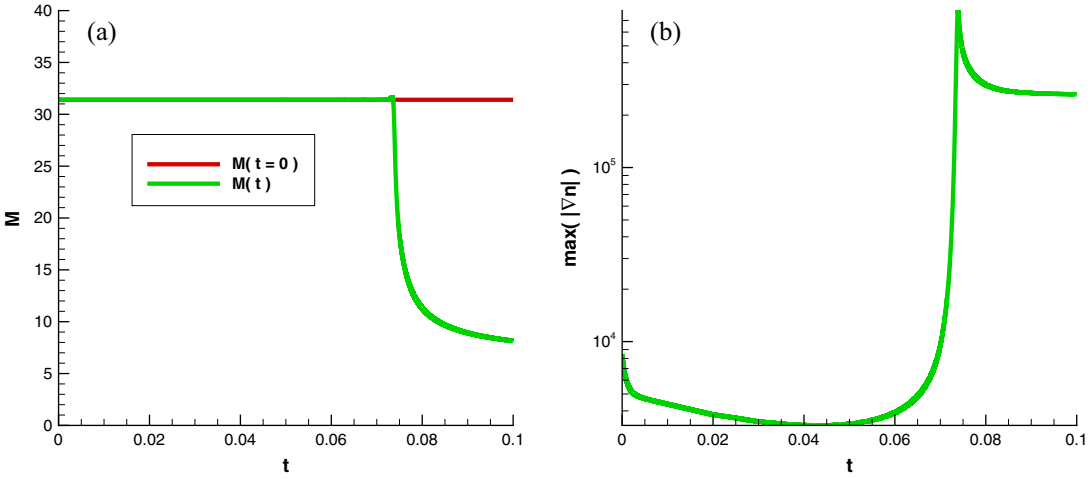

Fig. 8. (a) The predicted total mass $M = \int\int n(x, y, t)dx$; and (b) The predicted maximum value of ∇n along the line $x - y = 0$ is plotted with respect to time.

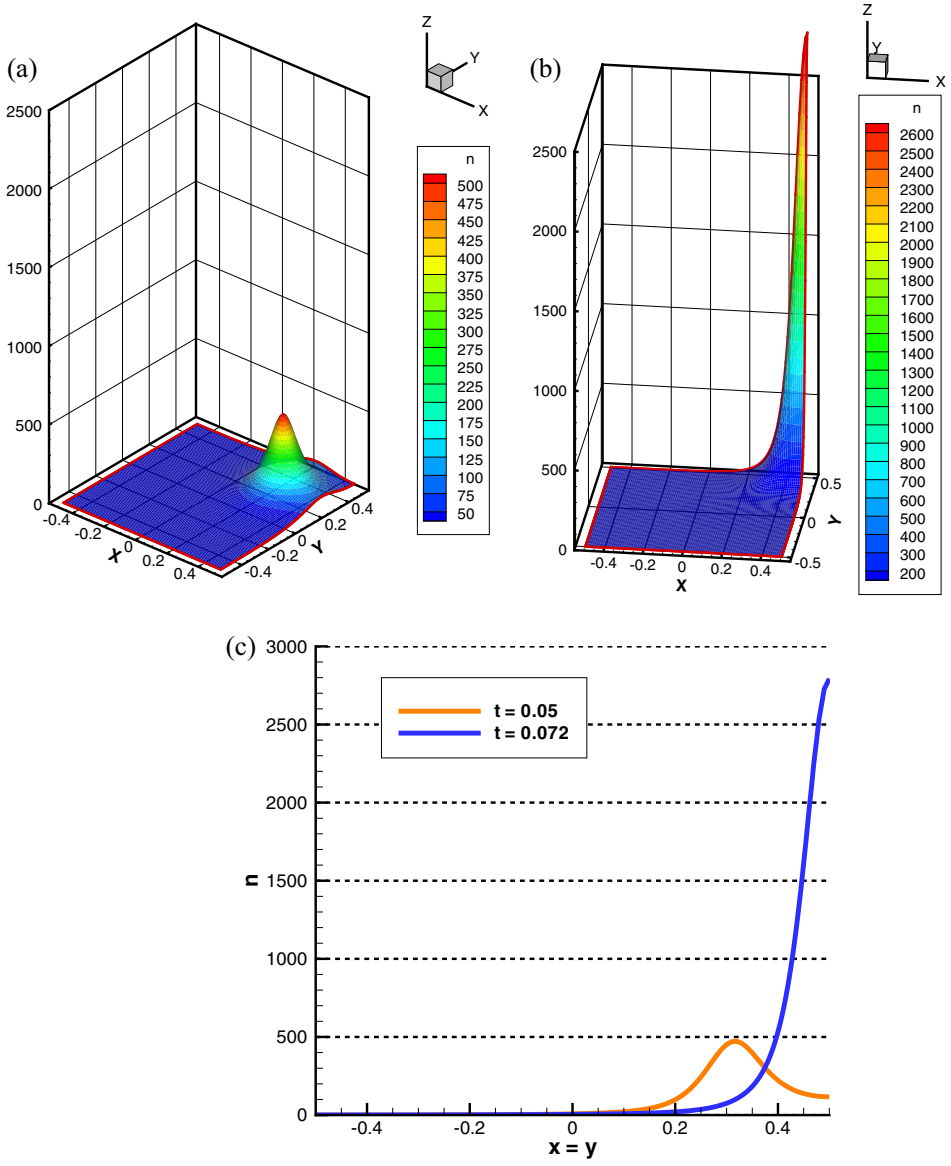

Fig. 9. The simulated distribution of n solutions along the line $x - y = 0$ at $t = 0.02$ and $t = 0.072$. (a) three-dimensional view of the predicted value of n at $t = 0.02$; and (b) three-dimensional view of the predicted value of n at $t = 0.072$; (c) the predicted distribution of $n(x, t)$ solutions along the line $x - y = 0$.

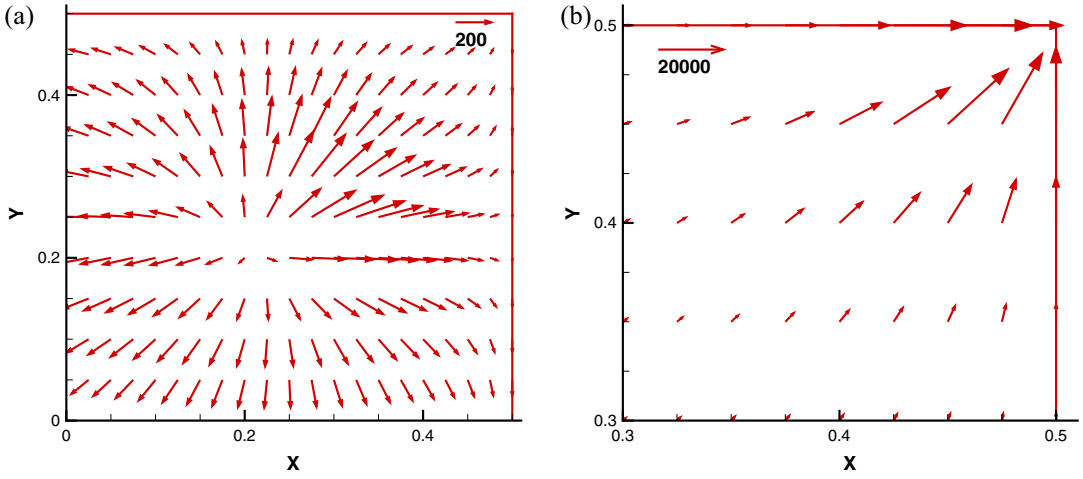

Fig. 10. The predicted total flux vector for the case with $U_{max} = 0$ in the upper right square $0 \leqslant x, y \leqslant 0.5$ and $0.3 \leqslant x, y \leqslant 0.5$. (a) total flux computed at $t = 0.0128$; and (b) total flux computed at $t = 0.072$.

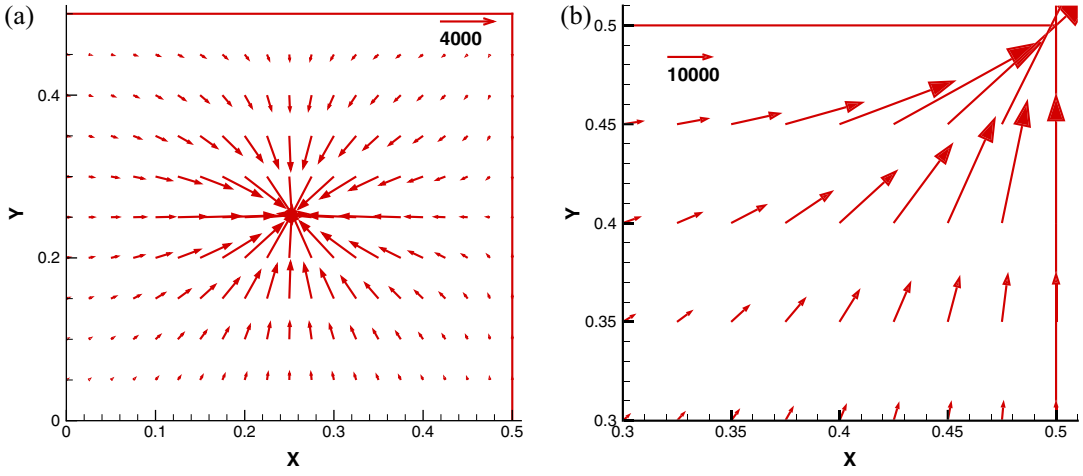

Fig. 11. The predicted chemotaxic force vectors for the case with $U_{max} = 0$ in the upper right square $0 \leqslant x, y \leqslant 0.5$ and $0.3 \leqslant x, y \leqslant 0.5$. (a) the chemotaxic force vector predicted at $t = 0.0128$; and (b) the chemotaxic force vector predicted at $t = 0.072$.

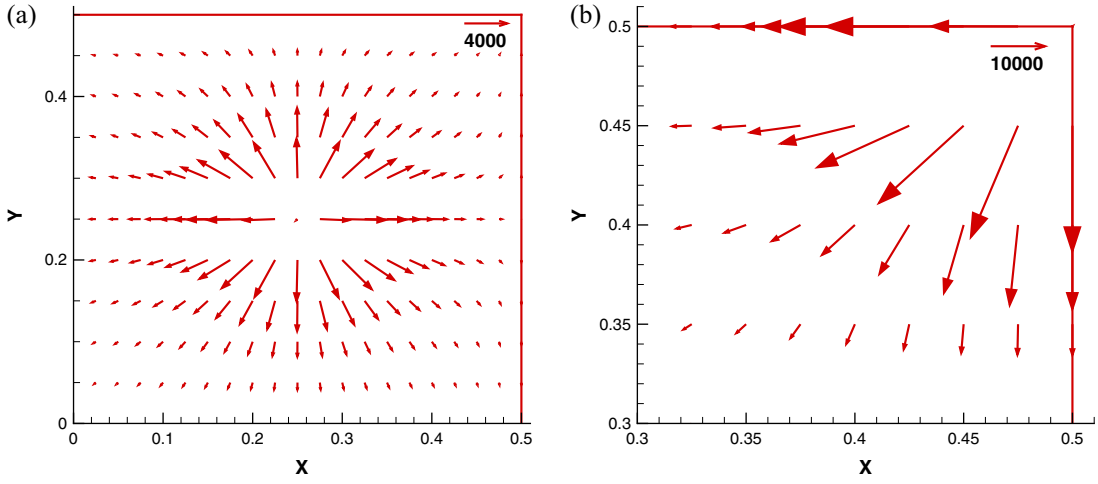

Fig. 12. The predicted diffusion flux vectors for the case investigated at $U_{max} = 0$ in the upper right square $0 \leqslant x, y \leqslant 0.5$ and $0.3 \leqslant x, y \leqslant 0.5$. (a) the diffusion force vector predicted at $t = 0.0128$; and (b) the diffusion force vector predicted at $t = 0.072$.

On the right hand side of Eq. (1), the vector $\underline{J}$ [$ML^{-2}\ T^{-1}$] denotes the current generated by chemotaxis. This flux term accounts for the chemotaxis-driven motion and its formation has relevance to the spatially non-uniform distributed oxygen concentration c in the following way

$$\underline{J} = \chi n \nabla c. \tag{3}$$

The chemotactic coefficient $\chi(c)$ [$M^{-1}\ L^5\ T^{-1}$] shown in Eq. (3) decreases very often with the chemoattractant concentration c. It is worthy to address here that the gradient term ∇c accounts for the characteristic motion of bacteria moving along the direction of chemical (oxygen in this study) concentration gradient. In summary, the time rate of the change of the bacterium density $\frac{Dn}{Dt}$ $(\equiv \frac{\partial n}{\partial t} + \underline{u} \cdot \nabla n)$ in a fluid flow is governed by the diffusion effect $\nabla^2 n$ and the chemotaxic current $\underline{J}$ in the direction of oxygen gradient. Beside the diffusion and convection effects in the oxygen flow, the fact that bacteria can consume oxygen must be taken into account when modeling oxygen transport processes. The uptake of oxygen by bacteria should be included in Eq. (2).

Provided that there is no flow motion, the biological Eqs. (1) and (2) turn out to be the celebrated Patlak-Keller-Segel (PKS) equations. The Patlak-Keller-Segel parabolic model has been obtained at the diffusion limit [7,8]. In other words, the propagation of cells in PKS model is controlled entirely by the diffusion process. Existence and uniqueness of the finite volume solution for the parabolic PKS equations has been proven in [10]. Provided that the initial mass is smaller than the threshold value, convergent solution to the PKS system was also revealed in the same article. The recent research addresses the development of hyperbolic model for chemotaxis [9,12]. This hyperbolic system of equations for chemosensitive movement takes the population flux of cell into account and respects the finite propagation speed of cells. This physically more complex model has been solved numerically by the finite volume method in [11].

To better understand the effect of chemotaxis in the original PKS equations, Eq. (1) investigated under a velocity-free condition can be rewritten as $\frac{\partial n}{\partial t} + \nabla \cdot (\chi n \nabla c) = \nabla^2 n$. By introducing the vector field (u^*, v^*), defined as ∇c, the transport equation for n at $\chi = 1$, for example, can be rewritten to the following convection–diffusion-reaction (CDR) equation

$$\frac{\partial n}{\partial t} + u^* \frac{\partial n}{\partial x} + v^* \frac{\partial n}{\partial y} - (n_{xx} + n_{yy}) + (c_{xx} + c_{yy})\ n = 0. \tag{4}$$

Thanks to the above derived CDR equation obtained at $\chi = 1$, chemical concentration is known to have an effect on the time-evolving cell density n not only by way of advection (or $(u^*, v^*) \cdot \nabla n$) but also

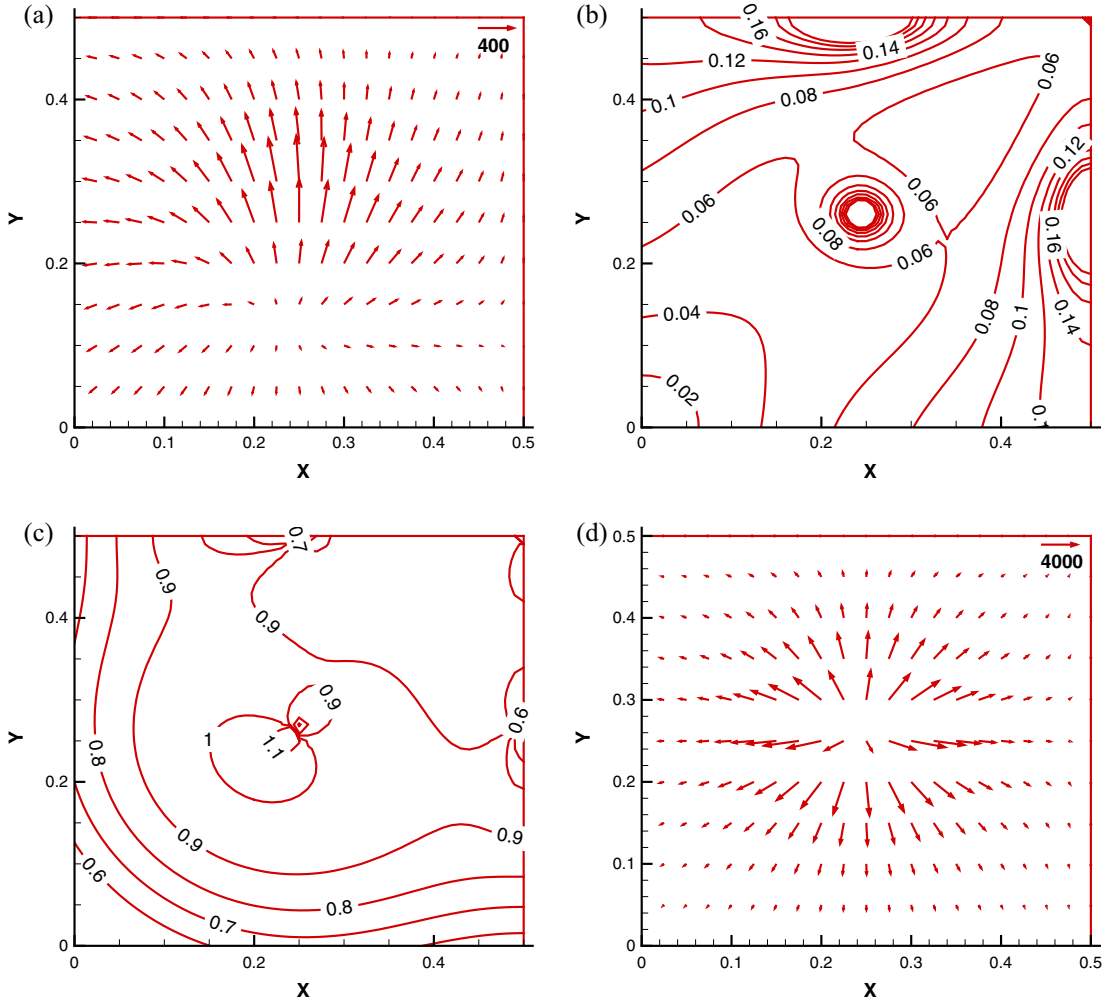

Fig. 13. The predicted ratios of $\frac{|\mathbf{un}|}{|\nabla n|}$ and $\frac{|n\nabla c|}{|\nabla n|}$ at $t = 0.016$ for the case investigated at $U_{max} = 1$. (a) total flux vector; (b) contours of the ratio $\frac{|\mathbf{un}|}{|\nabla n|}$; (c) contours of the ratio $\frac{|n\nabla c|}{|\nabla n|}$; and (d) the dominant vector in $\underline{F}$, which is the diffusion force vector.

by virtue of reaction with the amount of $\nabla^2 c$. Because of the convection-like term shown in Eq. (4), one should apply a scheme of upwinding type to model the time-evolving cell density n so as to properly smooth-out or resolve the possible numerical convective instabilities [6].

Due to the convective flux terms $\underline{u}\cdot\nabla n$ and $\underline{u}\cdot\nabla c$ included in the current simulation of chemotaxic processes, the hydrodynamic equations for an incompressible viscous fluid flow must be coupled with the transport equations for the cell density n in (1) and the chemical concentration c in (2). The gravitational force is modeled by $\nabla\Phi(\equiv(0, V_b n_r g(\rho_0-\rho))$. The resulting set of the elliptic–parabolic equations given below will be solved subject to the problem-dependent initial and boundary conditions

$$\nabla\cdot\underline{u}' = 0, \tag{5}$$

$$\frac{\partial \underline{u}'}{\partial t'} + \underline{u}'\cdot\nabla\underline{u}' = \mathbf{S}c\nabla^2\underline{u}' - \mathbf{S}c\nabla p' - n'\nabla\Phi', \tag{6}$$

$$\frac{\partial n'}{\partial t'} + \underline{u}'\cdot\nabla n' = \nabla^2 n' - \alpha\nabla\cdot[\mathbf{r}(c')n'\nabla c'], \tag{7}$$

$$\frac{\partial c'}{\partial t'} + \underline{u}'\cdot\nabla c' = \delta\nabla^2 c' - \beta\mathbf{r}(c')n'. \tag{8}$$

The above dimensionless equations result from the normalization of equations using the chosen characteristic length $x' = \frac{x}{L}$, time $t' = \frac{D_n}{L^2}t$, velocity $\underline{u}' = \frac{L}{D_n}\underline{u}$, pressure $p' = \frac{L^2}{\eta D_n}p$, cell density $n' = \frac{n}{n_r}$, chemical concentration $c' = \frac{c}{c_{air}}$, and gravitational force $\nabla\Phi' = (0, \frac{\eta V_b n_r g(\rho_0-\rho)L^3}{D_n\rho})$. Normalization of the four equations leads to $\mathbf{S}c = \frac{\eta}{D_n\rho}$, $\alpha = \frac{\chi c_{air}}{L}$, $\beta = \frac{\kappa n_r L^2}{c_{air}D_n}$, $\gamma = \frac{V_b n_r g(\rho_0-\rho)L^3}{\eta D_n}$ and $\delta = \frac{D_c}{D_n}$. In what follows, the superscript " ' " shown in (5)–(8) is omitted for brevity. Note that the transport equations for u', n', and c'can be recast into a general form as $\phi_t + a\phi_x + b\phi_y + c\phi = k\nabla^2\phi + f$. The coefficients a, b, c, k and the source term f are tabulated in Table 1.

3. Numerical method

After approximating ϕ_t using the Euler time-stepping scheme for the model equation $\phi_t + a\ \phi_x + b\ \phi_y + c\ \phi = k\ \nabla^2\phi + f$, which represents the Eqs. (6)–(8) shown in the previous section, the semi-discretized equation is derived as follows for $\overline{\phi}(\equiv\phi\Delta t)$, where $\overline{f} = f\Delta t + \phi^n$ and $c^* = c + \frac{1}{\Delta t}$

$$a\frac{\partial\overline{\phi}}{\partial x}\Big|^n + b\frac{\partial\overline{\phi}}{\partial y}\Big|^n - k\left(\frac{\partial^2\overline{\phi}}{\partial x^2}\Big|^n + \frac{\partial^2\overline{\phi}}{\partial y^2}\Big|^n\right) + c^*\overline{\phi}\Big|^{n+1} = \overline{f}\Big|^{n+1}. \tag{9}$$

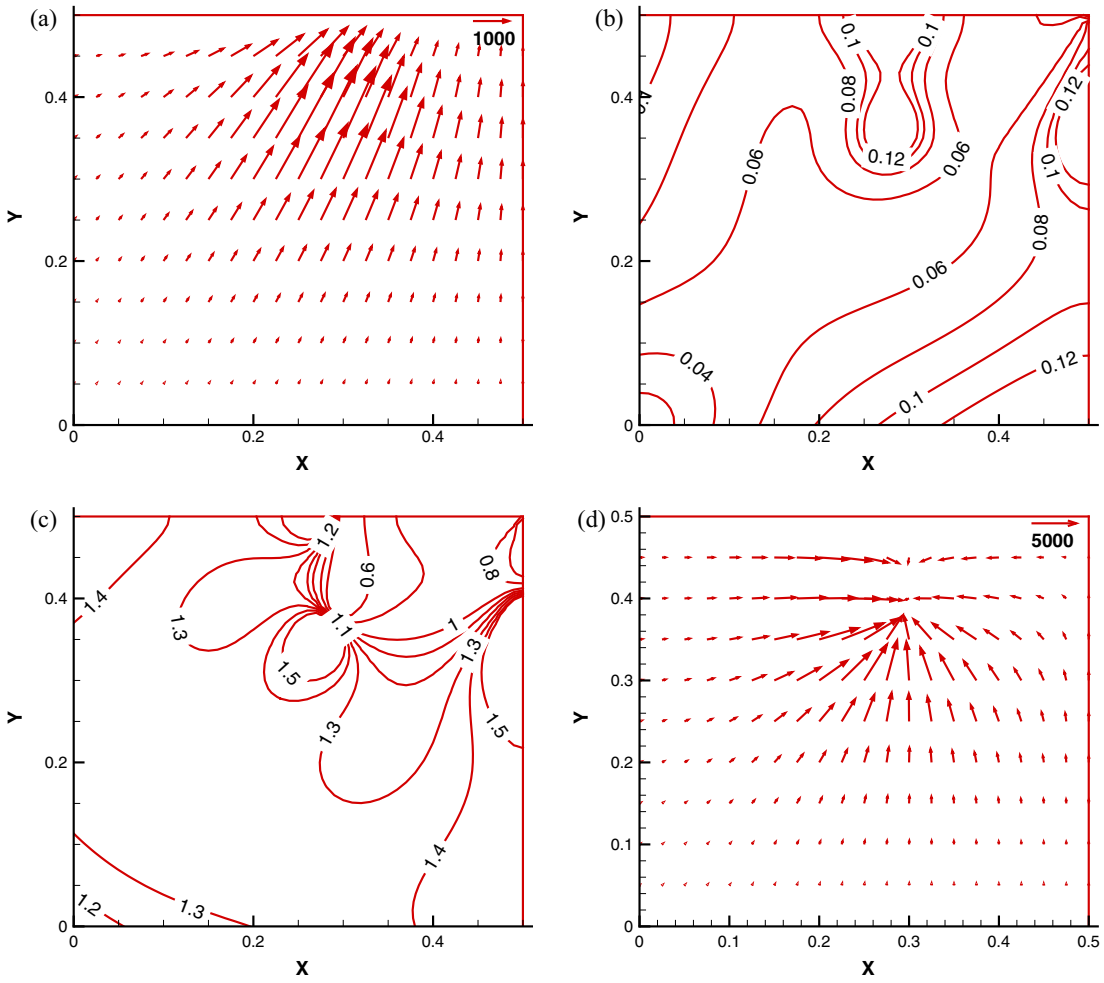

Fig. 14. The predicted ratios of $\frac{|\mathbf{un}|}{|\nabla n|}$ and $\frac{|n\nabla c|}{|\nabla n|}$ at $t = 0.0528$ for the case investigated at $U_{max} = 1$. (a) total flux vector; (b) contours of the ratio $\frac{|\mathbf{un}|}{|\nabla n|}$; (c) contours of the ratio $\frac{|n\nabla c|}{|\nabla n|}$; and (d) the dominant vector in $\underline{F}$, which is the chemotaxic force vector.

In the above, the coefficients a and b are denoted as the constant velocities along the respective x- and y-direction, k the constant diffusion coefficient, and f the source term. The first-order and second-order spatial derivative terms shown in Eq. (9) are both approximated in a mesh of constant grid spacing $\Delta x = \Delta y = h$.

The first-order derivative term $\frac{\partial \overline{\phi}}{\partial x}$ and the second-order derivative term $\frac{\partial^2 \overline{\phi}}{\partial x^2}$ in Eq. (9) at the same time $n\Delta t$ are approximated below within the combined compact difference context in a three-point stencil

$$a_1 \frac{\partial \overline{\phi}}{\partial x}|_{i-1} + \frac{\partial \overline{\phi}}{\partial x}|_i = \frac{1}{h}(c_1 \overline{\phi}_{i-1} + c_2 \overline{\phi}_i + c_3 \overline{\phi}_{i+1}) - h\left(b_1 \frac{\partial^2 \overline{\phi}}{\partial x^2}|_{i-1} + b_2 \frac{\partial^2 \overline{\phi}}{\partial x^2}|_i + b_3 \frac{\partial^2 \overline{\phi}}{\partial x^2}|_{i+1}\right), \tag{10}$$

$$\overline{b}_1 \frac{\partial^2 \overline{\phi}}{\partial x^2}|_{i-1} + \frac{\partial^2 \overline{\phi}}{\partial x^2}|_i + \overline{b}_3 \frac{\partial^2 \overline{\phi}}{\partial x^2}|_{i+1} = \frac{1}{h^2}(\overline{c}_1 \overline{\phi}_{i-1} + \overline{c}_2 \overline{\phi}_i + \overline{c}_3 \overline{\phi}_{i+1}) - \frac{1}{h}\left(\overline{a}_1 \frac{\partial \overline{\phi}}{\partial x}|_{i-1} + \overline{a}_2 \frac{\partial \overline{\phi}}{\partial x}|_i + \overline{a}_3 \frac{\partial \overline{\phi}}{\partial x}|_{i+1}\right). \tag{11}$$

The other two terms $\frac{\partial \overline{\phi}}{\partial y}$ and $\frac{\partial^2 \overline{\phi}}{\partial y^2}$ can be similarly expressed along the y-direction. Note that the combined compact representations of $\frac{\partial \overline{\phi}}{\partial x}|_i$ and $\frac{\partial^2 \overline{\phi}}{\partial x^2}|_i$ are coupled with each other through the terms $\frac{\partial \overline{\phi}}{\partial x}|_{i-1}$, $\frac{\partial \overline{\phi}}{\partial x}|_i$, $\frac{\partial \overline{\phi}}{\partial x}|_{i+1}$, $\frac{\partial^2 \overline{\phi}}{\partial x^2}|_{i-1}$, $\frac{\partial^2 \overline{\phi}}{\partial x^2}|_i$, $\frac{\partial^2 \overline{\phi}}{\partial x^2}|_{i+1}$, $\overline{\phi}_{i-1}$, $\overline{\phi}_i$ and $\overline{\phi}_{i+1}$. For ease of description of the present numerical method, only the case involving positive convective coefficients is derived below in detail.

The second-order derivative terms are normally approximated using the centered schemes. As a result, for getting a better spatial accuracy the weighting coefficients shown in Eq. (11) are determined solely from the modified equations analysis. Derivation of $\overline{a}_1$, $\overline{a}_2$, $\overline{a}_3$, $\overline{b}_1, \overline{b}_3$, $\overline{c}_1$, $\overline{c}_2$, and $\overline{c}_3$ in (10) and (11) is started with performing the Taylor series expansions for $\overline{\phi}_{i\pm1}, \frac{\partial \overline{\phi}}{\partial x}|_{i\pm1}$ and $\frac{\partial^2 \overline{\phi}}{\partial x^2}|_{i\pm1}$ with respect to $\overline{\phi}_i, \frac{\partial \overline{\phi}}{\partial x}|_i$ and $\frac{\partial^2 \overline{\phi}}{\partial x^2}|_i$. The leading error terms derived in the modified equations are then eliminated. Elimination of the eight leading error terms shown in the modified equation enables us to get the eight algebraic equations for Eq. (11). By solving these equations, the coefficients shown in Eq. (11) are derived as $\overline{a}_1 = -\frac{9}{8}$, $\overline{a}_2 = 0$, $\overline{a}_3 = \frac{9}{8}$, $\overline{b}_1 = -\frac{1}{8}$, $\overline{b}_3 = -\frac{1}{8}$, $\overline{c}_1 = 3$, $\overline{c}_2 = -6$, $\overline{c}_3 = 3$. The resulting derived modified equation for $\frac{\partial^2 \overline{\phi}}{\partial x^2}$, which is $\frac{\partial^2 \overline{\phi}}{\partial x^2} = \frac{\partial^2 \overline{\phi}}{\partial x^2}|_{exact} + \frac{h^6}{20160}\frac{\partial^8 \overline{\phi}}{\partial x^8} + \frac{h^8}{604800}\frac{\partial^{10} \overline{\phi}}{\partial x^{10}} + O(h^{12}) + \cdots$, clearly shows that the proposed scheme for $\frac{\partial^2 \overline{\phi}}{\partial x^2}$ has the spatial accuracy of order six.

The coefficients a_1, $b_1 \sim b_3$, $c_1 \sim c_3$ are partly determined as before by expanding the terms $\phi_{i\pm1}, \frac{\partial \phi}{\partial x}|_{i-1}$ and $\frac{\partial^2 \phi}{\partial x^2}|_{i\pm1}$ in Taylor series with respect to $\phi_i, \frac{\partial \phi}{\partial x}|_i$ and $\frac{\partial^2 \phi}{\partial x^2}|_i$, respectively. By eliminating the

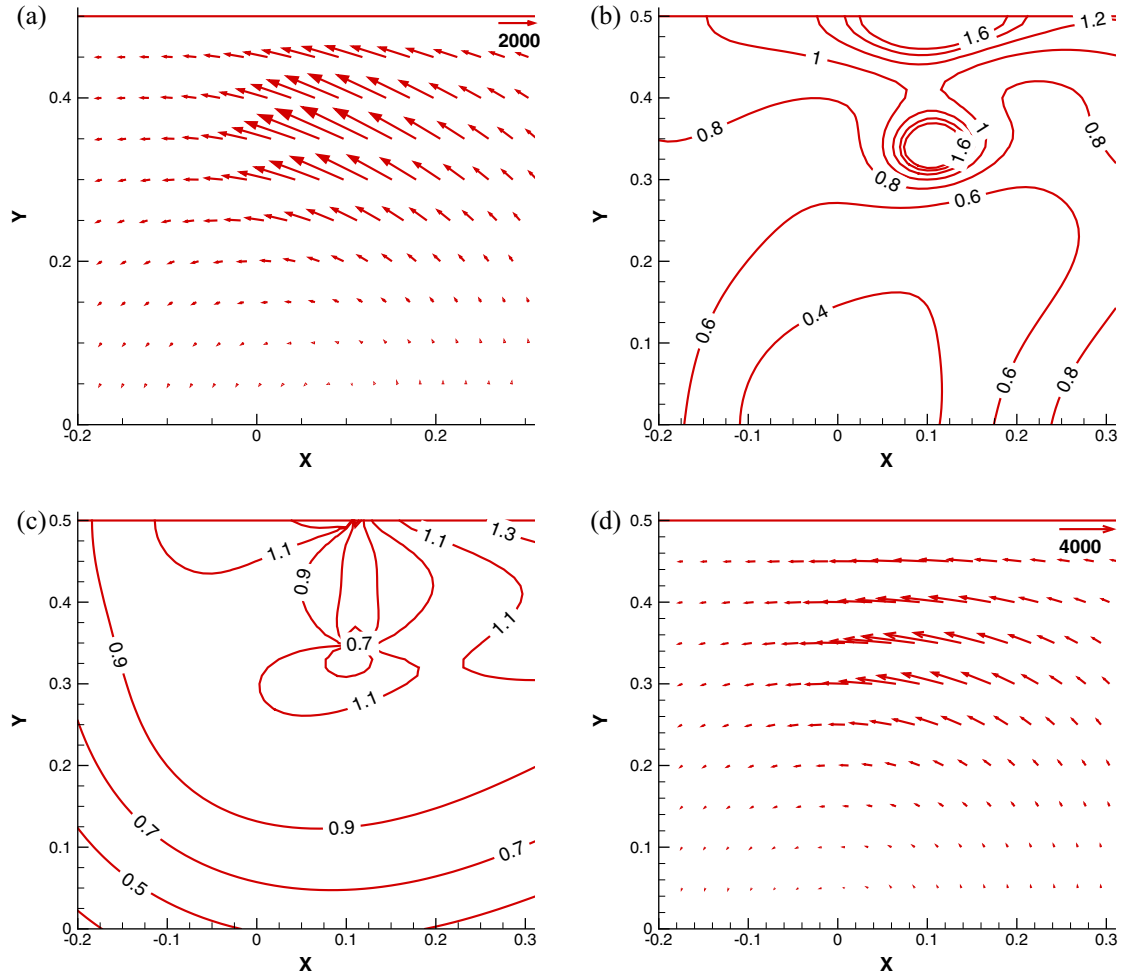

Fig. 15. The predicted ratios of $\frac{|\mathbf{un}|}{|\nabla n|}$ and $\frac{|n\nabla c|}{|\nabla n|}$ at $t = 0.0224$ for the case investigated at $U_{max} = 10$. (a) total flux vector; (b) contours of the ratio $\frac{|\mathbf{un}|}{|\nabla n|}$; (c) contours of the ratio $\frac{|n\nabla c|}{|\nabla n|}$; and (d) the dominant force vector in F, which is the convection force vector.

leading error terms derived in the modified equation, the following set of equations for Eq. (10) can be derived

$$c_1 + c_2 + c_3 = 0, \tag{12}$$
$$-a_1 - c_1 + c_3 = 1, \tag{13}$$
$$-a_1 + b_1 + b_2 + b_3 - \frac{c_1}{2} - \frac{c_3}{2} = 0, \tag{14}$$
$$\frac{a_1}{2} - b_1 + b_3 + \frac{c_1}{6} - \frac{c_3}{6} = 0, \tag{15}$$
$$-\frac{a_1}{6} + \frac{b_1}{2} + \frac{b_3}{2} - \frac{c_1}{24} - \frac{c_3}{24} = 0, \tag{16}$$
$$\frac{a_1}{24} - \frac{b_1}{6} + \frac{b_3}{6} + \frac{c_1}{120} - \frac{c_3}{120} = 0. \tag{17}$$

One more algebraic equation is needed for us to uniquely determine all the seven introduced coefficients shown in Eq. (10).

For accurately approximating the first-order derivative term from Eq. (10), the dispersive nature embedded in $\frac{\partial \phi}{\partial x}$ must be well retained. To preserve the dispersion nature, the Fourier transform and its inverse for ϕ given below are applied

$$\tilde{\phi}(\alpha) = \frac{1}{2\pi} \int_{-\infty}^{+\infty} \phi(x) \exp(-\mathbf{i}\alpha x)\, dx, \tag{18}$$
$$\phi(x) = \int_{-\infty}^{+\infty} \tilde{\phi}(\alpha) \exp(\mathbf{i}\alpha x)\, d\alpha. \tag{19}$$

The notation $\mathbf{i}$ shown above is equal to $\sqrt{-1}$. A dispersively accurate scheme for the first-order derivative term can be developed by performing Fourier transform on each term shown in Eqs. (10) and (11). The expressions of the exact wavenumber α for these two equations can be therefore derived. The effective wavenumbers α' and α'' are then equated to the exact wavenumber to get the following equations for α' and α''

$$\begin{aligned}\mathbf{i}\alpha' h(a_1 \exp(-\mathbf{i}\alpha h) + 1) = {} & c_1 \exp(-\mathbf{i}\alpha h) + c_2 + c_3 \exp(\mathbf{i}\alpha h) \\ & - (\mathbf{i}\alpha'' h)^2 (b_1 \exp(-\mathbf{i}\alpha h) + b_2 + b_3 \\ & \times \exp(\mathbf{i}\alpha h)),\end{aligned} \tag{20}$$

$$\begin{aligned}&\mathbf{i}\alpha' h\left(-\frac{8}{9}\exp(-\mathbf{i}\alpha h) + \frac{8}{9}\exp(\mathbf{i}\alpha h)\right) \\ &= 3\exp(-\mathbf{i}\alpha h) - 6 + 3\exp(\mathbf{i}\alpha h) \\ &\quad - (\mathbf{i}\alpha'' h)^2 \left(-\frac{1}{8}\exp(-\mathbf{i}\alpha h) + 1 - \frac{1}{8}\exp(\mathbf{i}\alpha h)\right).\end{aligned} \tag{21}$$

By solving the above two equations, the expressions for α' and α'' can be derived [13]. To get a better dispersive accuracy for α', it is demanded that $\alpha h \approx \Re[\alpha' h]$, where $\Re[\alpha' h]$ denotes the real part of

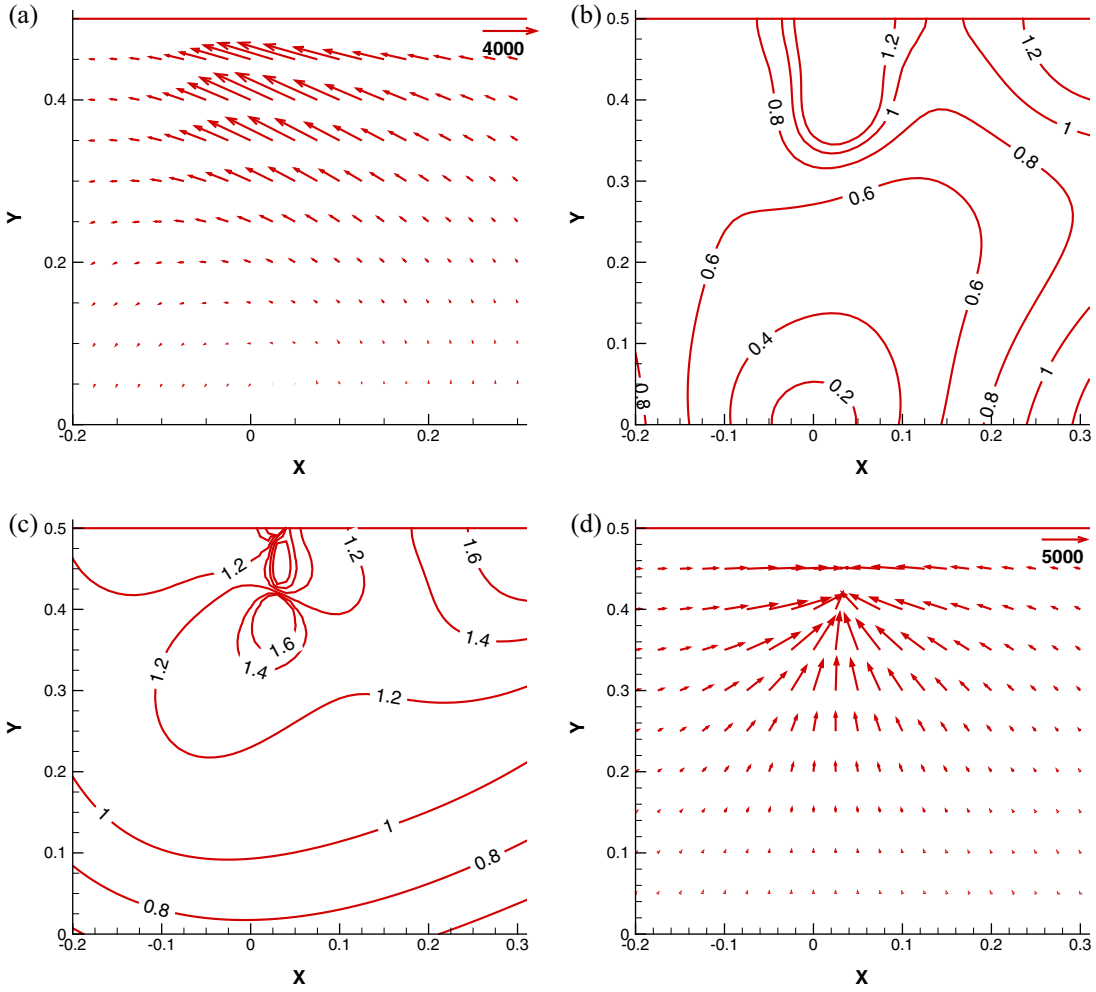

Fig. 16. The predicted ratios of $\frac{|\mathbf{u}n|}{|\nabla n|}$ and $\frac{|n\nabla c|}{|\nabla n|}$ at $t = 0.032$ for the case investigated at $U_{max} = 10$. (a) total flux vector; (b) contours of the ratio $\frac{|\mathbf{u}n|}{|\nabla n|}$; (c) contours of the ratio $\frac{|n\nabla c|}{|\nabla n|}$; and (d) the dominant vector in $\underline{F}$, which is the chemotaxic force vector.

$\alpha' h$. The value of $E(\alpha)$ defined below should be very small and positive

$$E(\alpha) = \int_{-\frac{\pi}{2}}^{\frac{\pi}{2}} [W(\alpha h - \Re[\alpha' h])]^2 d(\alpha h) = \int_{-\frac{\pi}{2}}^{\frac{\pi}{2}} [W(\gamma - \Re[\gamma'])]^2 d\gamma, \quad (22)$$

where $\gamma = \alpha h$ and $\gamma' = \alpha' h$. To integrate the above equation exactly, one trivial way can be chosen is to set W as the denominator of the above integral.

The function E defined in Eq. (22) has a positive and minimum value provided that the following extreme condition is enforced

$$\frac{\partial E}{\partial c_3} = 0. \quad (23)$$

The equation implemented to preserve dispersion relation is used together with other six previously derived algebraic equations through the modified equation analysis to get a smaller dissipation error and render a better dispersion accuracy. The resulting seven introduced unknowns can be therefore uniquely determined as $a_1 = 0.875, b_1 = 0.12512823, b_2 = -0.24871766, b_3 = 0.00012823415, c_1 = -1.93596119, c_2 = 1.99692238, c_3 = -0.06096119$. Given the above coefficients, the developed upwinding scheme for $\frac{\partial \phi}{\partial x}$ can be easily shown to have the spatial accuracy of order five from the modified equation derived as

$$\frac{\partial \phi}{\partial x} = \frac{\partial \phi}{\partial x}|_{exact} - 0.0007009h^5 \frac{\partial^6 \phi}{\partial x^6} + 0.0001984h^6 \frac{\partial^7 \phi}{\partial x^7} - 0.0000499h^7 \frac{\partial^8 \phi}{\partial x^8} + O(h^8) + \cdots$$

In this paper, one-sided difference scheme for the problems subject to Neumann-type boundary conditions in Sections 4 and 5 is employed. One can refer to our previous paper [14] for details about the derivation of compact scheme of fourth-order accuracy for Neumann-type boundary condition.

Calculation of the hydrodynamic equations begins with solving the following two equations in the projection step

$$\frac{\underline{u}^{n+1} - \underline{u}^{n+\frac{1}{2}}}{\Delta t} = -\nabla p^{n+1}, \quad (24)$$

$$\nabla \cdot \underline{u}^{n+1} = 0. \quad (25)$$

Substitution of Eq. (24) into the semi-discretized momentum equation leads to

$$\frac{\underline{u}^{n+1} - \underline{u}^{n}}{\Delta t} + (\underline{u}^{n+\frac{1}{2}} \cdot \nabla)\underline{u}^{n+\frac{1}{2}} - \frac{1}{Re}\nabla^2 \underline{u}^{n+\frac{1}{2}} + \nabla p^{n+1} = M_1 + M_2. \quad (26)$$

In the above, $M_1 = [(\underline{u}^{n+\frac{1}{2}} \cdot \nabla)\nabla p^{n+1} + (\nabla p^{n+1} \cdot \nabla)\underline{u}^{n+\frac{1}{2}} - \frac{1}{Re}\nabla^2(\nabla p^{n+1})]\Delta t$ and $M_2 = -[(\nabla p^{n+1} \cdot \nabla)\nabla p^{n+1}]\Delta t^2$. Let $p^{n+1} = p^* + p'$, the pressure-gradient step is decomposed into the solution step containing the equation $\frac{\underline{u}^* - \underline{u}^{n+\frac{1}{2}}}{\Delta t} = -\nabla p^*$ and the other solution step

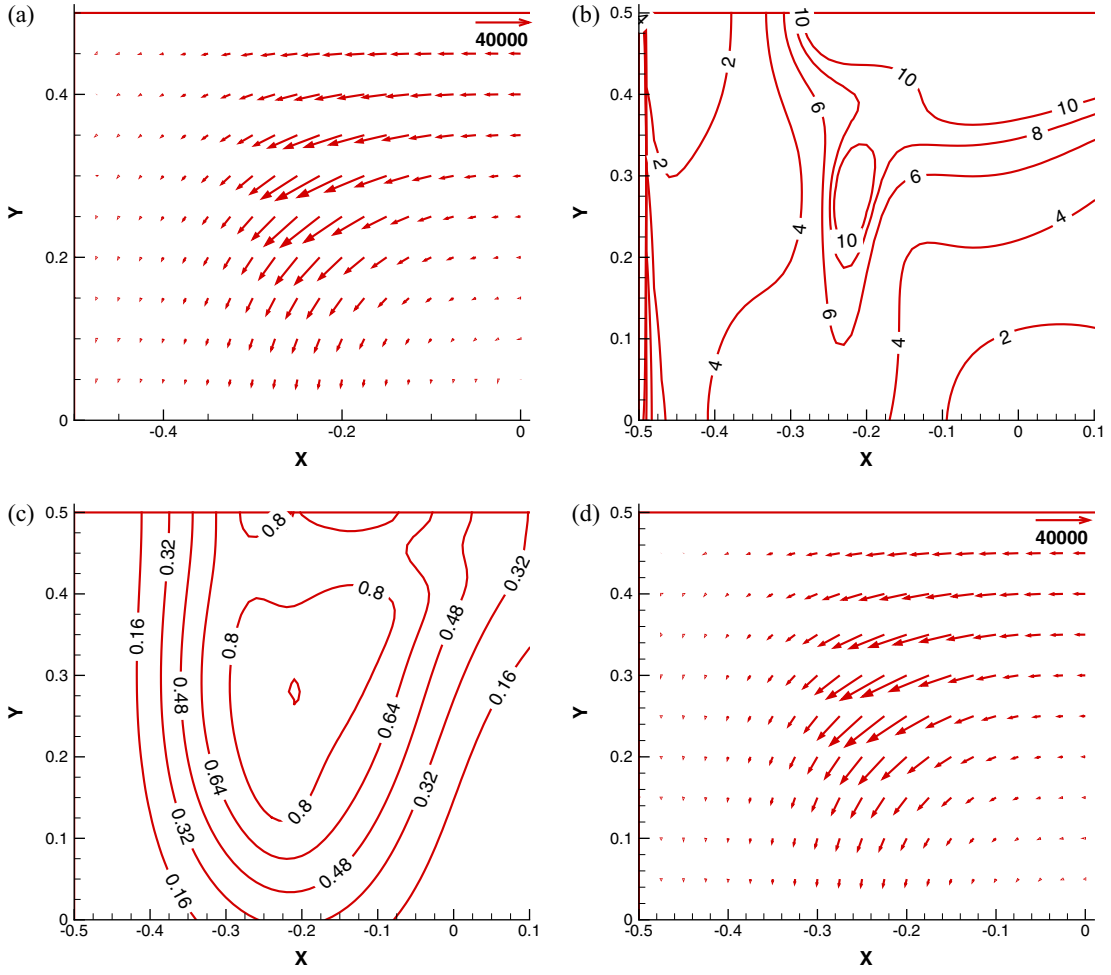

Fig. 17. The predicted ratios of $\frac{|\mathbf{un}|}{|\nabla n|}$ and $\frac{|n\nabla c|}{|\nabla n|}$ at $t = 0.0064$ for the case investigated at $U_{max} = 100$. (a) total flux vector; (b) contours of the ratio $\frac{|\mathbf{un}|}{|\nabla n|}$; (c) contours of the ratio $\frac{|n\nabla c|}{|\nabla n|}$; and (d) the dominant vector in $\underline{F}$, which is the convection force vector.

containing the equation $\frac{\underline{u}^{n+1}-\underline{u}^{*}}{\Delta t} = -\nabla p'$, where p^* is an intermediate pressure. Then, Eq. (26) can be reformulated as

$$\frac{\underline{u}^{n+1}-\underline{u}^{n}}{\Delta t} + (\underline{u}^{*}\cdot\nabla)\underline{u}^{*} - \frac{1}{Re}\nabla^2\underline{u}^{*} + \nabla p^{*} = -\nabla p' + M_3 + M_4, \quad (27)$$

where $M_3 = [(\underline{u}^{*}\cdot\nabla)\nabla p' + (\nabla p'\cdot\nabla)\underline{u}^{*}]\Delta t - \frac{1}{Re}\nabla(\nabla\cdot\underline{u}^{*})$ and $M_4 = -[(\nabla p'\cdot\nabla)\nabla p']\Delta t^2$. In order to reduce the computational cost, the algorithm proposed in [15] is employed.

4. Verification studies

4.1. Verification of the classical Keller-Segel equations

The classical Keller-Segel equations given below are solved for verifying the proposed numerical scheme

$$n_t = D_n\nabla^2 n - \nabla\cdot(\chi n\nabla c), \quad (28)$$

$$c_t = D_c\nabla^2 c + nf(c) - c\kappa. \quad (29)$$

In the above, D_n and D_c represent the diffusion constants with the units $[L^2T-1]$. The term $f(c)$ in Eq. (29) with the unit $[T^{-1}]$ denotes the cut-off function. For oxygen, the sign of the cut-off function is negative, while for carbon dioxide the sign is positive. The value of the chemical decay rate κ with the unit $[T^{-1}]$ depends on the chemical characteristics. The variable n, which represents the cell density or the bacterium concentration, has the unit $[ML^{-3}]$. As for the variable c, which denotes the concentration of the chemical, it has the unit $[ML^{-3}]$.

The above set of equations is solved at $D_n = D_c = \chi = f = k = 1$ in a square $0 \leqslant x, y \leq 1$. The KS equations are therefore simplified to the following two equations

$$n_t = \nabla^2 n - \nabla\cdot(n\nabla c), \quad (30)$$

$$c_t = \nabla^2 c + n - c. \quad (31)$$

Subject to the Neumann type boundary conditions $\frac{\partial n_{exact}}{\partial \underline{n}} = 0$ and $\frac{\partial c_{exact}}{\partial \underline{n}} = 0$, where $n_{exact} = e^{\pi^2 t}(\cos\pi x + \cos\pi y)$ and $c_{exact} = e^{\pi^2 t}(\cos\pi x + \cos\pi y)$, solutions will be sought at $\Delta t = 0.01(\Delta x)^2$ in five continuously refined meshes. Note that $\underline{n}$ represents the unit outward normal vector along the boundary. All the grid spacings are chosen to be much greater than Δt, thereby enabling us to get the spatial rate of convergence plotted in Fig. 1. The proposed combined compact difference scheme is verified because of these computed $L2$ error norms.

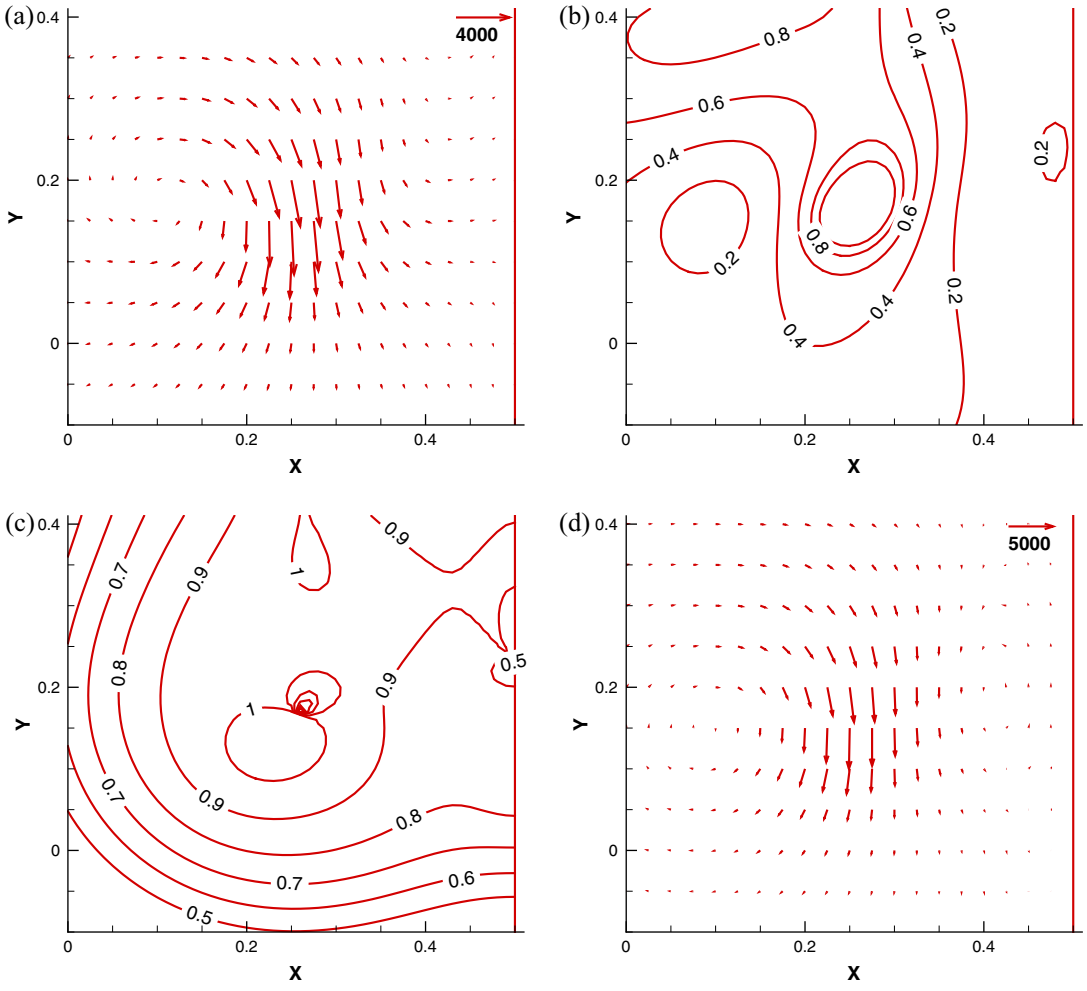

Fig. 18. The predicted ratios $\frac{|\underline{u}n|}{|\nabla n|}$ and $\frac{|n\nabla c|}{|\nabla n|}$ at $t = 0.016$. The initial maximum velocity is zero. (a) total flux vector; (b) contours of the predicted ratio $\frac{|\underline{u}n|}{|\nabla n|}$; (c) contours of the predicted ratio $\frac{|n\nabla c|}{|\nabla n|}$; and (d) the dominant vector in $\underline{F}$, which is the convection force vector.

4.2. Verification of the elliptic–parabolic Keller-Segel equations with the inclusion of convective terms

We then perform the second verification study by solving the following set of Keller-Segel equations which contains two convection terms $\underline{u}\cdot\nabla\underline{n}$ and $\underline{u}\cdot\nabla\underline{c}$, respectively

$$n_t + \underline{u}\cdot\nabla n = D_n\nabla^2 n - \nabla\cdot(\chi n\nabla c), \tag{32}$$

$$c_t + \underline{u}\cdot\nabla c = D_c\nabla^2 c + nf(c) - c\kappa. \tag{33}$$

As before, the Keller-Segel equations containing the convection, diffusion, and reaction terms are solved at $D_n = D_c = \chi = f = \kappa = 1$ in the prescribed divergence-free velocity flowfield ($u = -\pi\cos(\pi x)\sin(\pi y)e^{-2\pi^2 t}$, $v = \pi\sin(\pi x)\cos(\pi y)e^{-2\pi^2 t}$).

The results are sough subject to the Neumann conditions $\frac{\partial n_{exact}}{\partial \underline{n}} = 0$ and $\frac{\partial c_{exact}}{\partial \underline{n}} = 0$. The exact values of $n_{exact} = \cos(\pi x)\cos(\pi y)e^{-2\pi^2 t}$ and $c_{exact} = \cos(\pi x)\cos(\pi y)e^{-2\pi^2 t}$ are prescribed along the boundary of a square $0 \leqslant x, y \leqslant 1$ with the unit outward normal vector $\overline{n}$. Given the values $\Delta t = 0.01\Delta x^2$ and $\Delta x = \Delta y = 0.2, 0.1, 0.0625, 0.05$, the computed L_2 error norms and their corresponding spatial rates of convergence are plotted in Fig. 2. One can clearly see that the proposed scheme can accurately approximate the Eqs. (32) and (33) containing the convective terms.

4.3. Verification of the coupled NS–KS equations

After verifying the proposed scheme for solving the Keller-Segel equations with/without inclusion of convective terms, the following differential set accounting for the coupled Keller-Segel and incompressible viscous hydrodynamic equations is solved as well

$$\nabla\cdot\underline{u} = 0, \tag{34}$$

$$\frac{\partial \underline{u}}{\partial t} + \underline{u}\cdot\nabla\underline{u} = \mu\nabla^2\underline{u} - \nabla p, \tag{35}$$

$$n_t + \underline{u}\cdot\nabla n = D_n\nabla^2 n - \nabla\cdot(\chi n\nabla c), \tag{36}$$

$$c_t + \underline{u}\cdot\nabla c = D_c\nabla^2 c + nf(c) - c\kappa. \tag{37}$$

In this verification study, the physical properties are set as before at the constant values of $D_n = D_c = \chi = f = \kappa = 1$ in $0 \leqslant x, y \leqslant 1$. For the boundary conditions schematic as shown in Fig. 3 for u, v, n and c, Eqs. (34)–(37) are solved at $\Delta t = 0.01\Delta x^2$ in the continuously refined four meshes with $\Delta x = \Delta y = 0.2, 0.1, 0.0625, 0.05$. The predicted errors between the simulated and exact solutions, which are $u_{exact} = -\cos(\pi x)\sin(\pi y)e^{-2\pi^2 t}$, $v_{exact} = \sin(\pi x)\cos(\pi y)e^{-2\pi^2 t}$, $p = c_1 - 0.25(\cos(2\pi x) + \cos(2\pi y))e^{-4\pi^2 t}$, $n_{exact} = \cos(\pi x)\cos(\pi y)e^{-2\pi^2 t}$ and $c_{exact} = \cos(\pi x)\cos(\pi y)e^{-2\pi^2 t}$, are cast in their

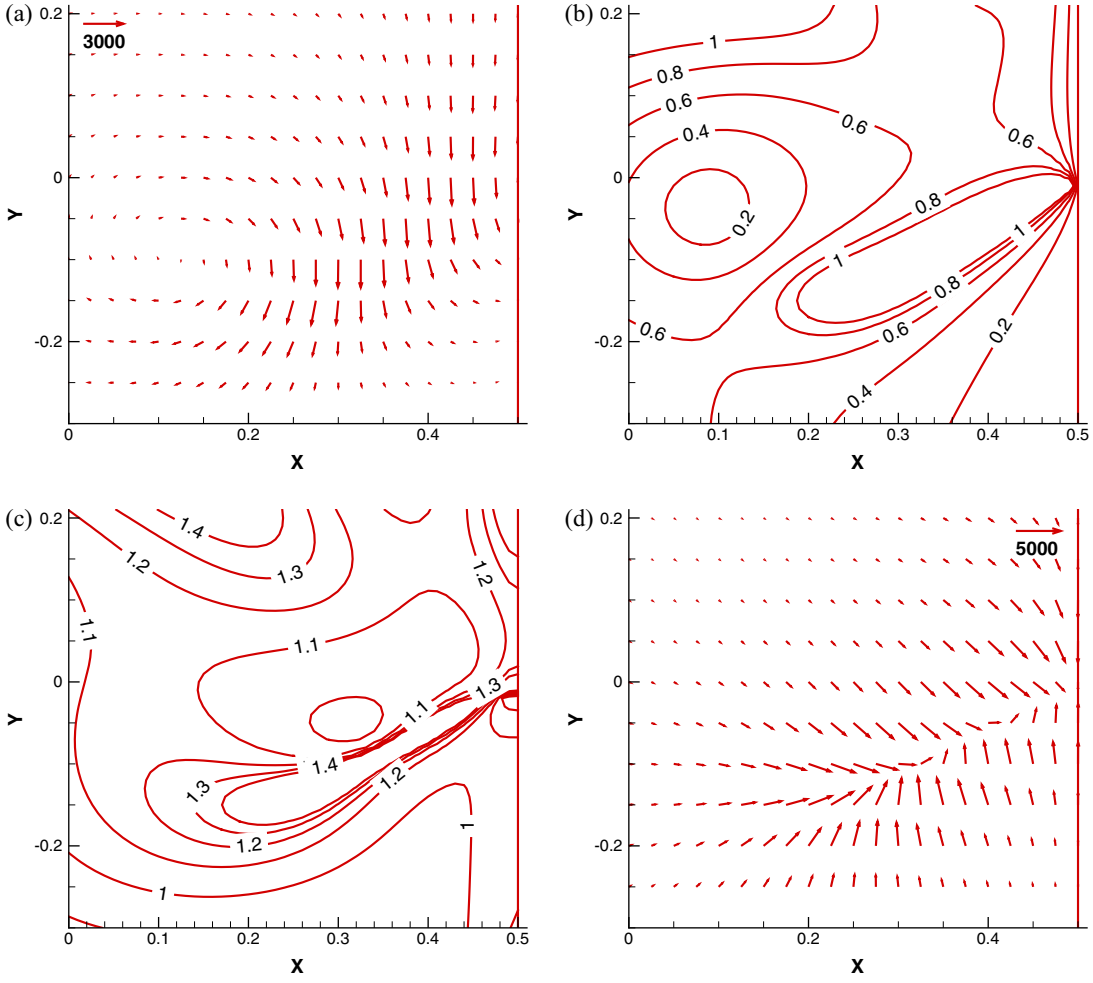

Fig. 19. The predicted ratios $\frac{|\underline{u}n|}{|\nabla n|}$ and $\frac{|n\nabla c|}{|\nabla n|}$ at $t = 0.068$. The initial maximum velocity is zero. (a) total flux vector; (b) contours of the predicted ratio $\frac{|\underline{u}n|}{|\nabla n|}$; (c) contours of the predicted ratio $\frac{|n\nabla c|}{|\nabla n|}$; and (d) the dominant vector in $\underline{F}$, which is the chemotaxic force vector.

L_2 – *norms*. From the predicted error norms, the spatial rates of convergence are plotted in Fig. 4. As before, good agreement between the exact and simulated results and states of convergence demonstrates the applicability of the proposed combined compact difference scheme and the flow solver described in Section 3 to investigate the chemotaxic phenomena in hydrodynamic environment.

5. Numerical results

5.1. Study of theoretical blow-up condition for the classical KS equations

Having successfully verified the scheme developed for the KS equations, this scheme will be applied to study the effect of initial condition on the possible blow-up solution in the classical Keller-Segel equations defined in an infinite domain [16]

$$n_t = \nabla^2 n - \nabla \cdot (n \nabla c), \tag{38}$$

$$c_t = \nabla^2 c + n - c. \tag{39}$$

The above two equations are solved subject to the initial conditions given as $n_o(t=0,\underline{x}) = 1300e^{-130(x^2+y^2)}$ and $c_0(t=0,\underline{x}) = 650e^{-65(x^2+y^2)}$. Note that this chosen initial solution for n corresponds to yield $\int_\Omega n_0 dxdy > 8\pi$. Subject to the specified boundary condition $\frac{\partial n}{\partial \hat{n}} = \frac{\partial c}{\partial \hat{n}} = 0$, the above set of KS equations is solved in the truncated square $-0.5 \leqslant x, y \leqslant 0.5$ rather in a computationally infeasible infinite domain. Note that the applied zero gradient boundary condition corresponds to the so-called zero-flux (or traction-free) boundary condition $\underline{n} \cdot (\nabla n - \chi n \nabla c) = \underline{n} \cdot \nabla c = 0$, where $\hat{n}$ denotes the unit outward normal vector. Our calculations are carried out at $\Delta t = 0.01\Delta x^2$ and $\Delta x = \Delta y = 0.0025$.

In Fig. 5, good comparison between the computed and referenced solutions is shown at two different times. The simulated solution gradient for n is seen to increase with time. Prior to $t = 5.39875 * 10^{-5}$, the increasingly sharper solution remains bounded without exhibiting blow-up phenomenon. At a time slightly beyond this critical time, the slope of the solution n shown in Fig. 6 becomes infinitely large. The distinguished blowup phenomenon which is known to occur in KS equations when $\int_\Omega n_0\, dxdy > 8\pi$ is numerically demonstrated in this study [17,18]. Such an increasingly larger gradient calls for an increase of grid points so as to be able to resolve the solution near the peak of solution occurring at the centroid of the solution domain. We found from this study that while solving the KS equations in a domain without a distinction of sufficiently finer grids, the total

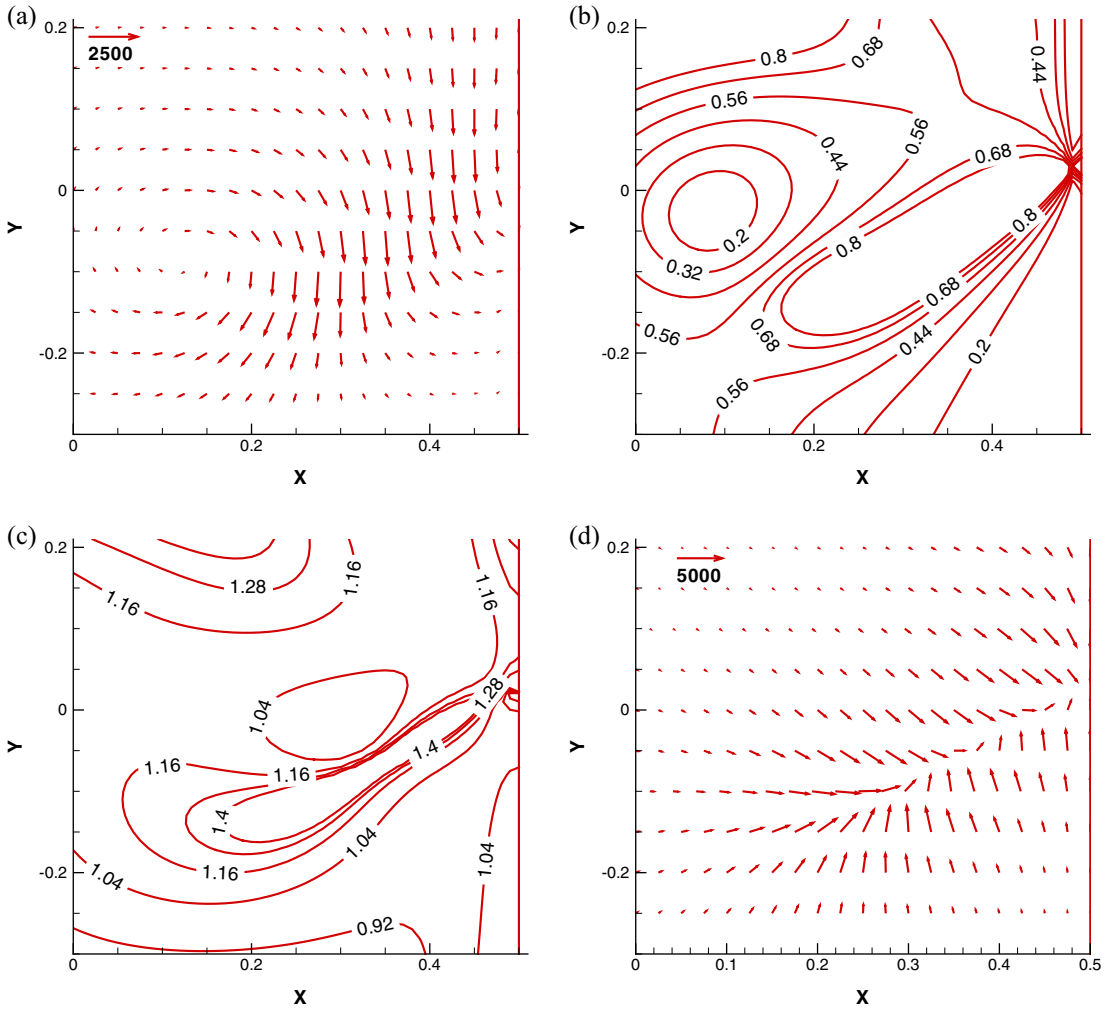

Fig. 20. The predicted ratios $\frac{|\mathbf{u}n|}{|\nabla n|}$ and $\frac{|n\nabla c|}{|\nabla n|}$ at $t = 0.072$. The initial maximum velocity is 1. (a) total flux vector; (b) contours of the predicted ratio $\frac{|\mathbf{u}n|}{|\nabla n|}$; (c) contours of the predicted ratio $\frac{|n\nabla c|}{|\nabla n|}$; and (d) the dominant vector in $\underline{F}$, which is the chemotaxic force vector.

mass within the physical domain can barely be conserved. The values of the total mass and the blowup time computed at different grid spacings for this problem are tabulated in Table 2.

The set of Eqs. (38) and (39) is also solved in the same square subject to the different set of initial conditions given as $n_o(t=0,\underline{x}) = 1000e^{-100[(x-0.25)^2+(y-0.25)^2]}$ and $c_0(t=0,\underline{x}) = 0$. The solutions at $t = 0.01785s$ computed under $\Delta x = \Delta y = 0.01$ and $\Delta t = 10^{-7}s$ are plotted in Fig. 7 for n at $t = 0.0625$ and 0.071875 and in Fig. 8 for the total mass $\int_\Omega n(x,t)dxdy$.

5.2. Effect of convection on the blow-up solution

In this section, the divergence-free steady-state velocity vector given by $u = -U_{max}cos(\pi x)sin(\pi y)$ and $v = U_{max}sin(\pi x)cos(\pi y)$ is added to the original Keller Segel equations as the convection term. The KS equations can be cast to the form given by $n_t + \nabla \cdot \underline{F} = 0$ so that each term shown in the total flux vector $\underline{F}$ given below can be individually analyzed

$$\underline{F} = \underline{u}n - D_n\nabla n + \chi n\nabla c. \tag{40}$$

Our aim is to know the roles of convection, diffusion, and chemotaxic terms on the time-evolving solution n. By changing the value of U_{max} in the specified velocity vector to yield different degrees of convective dominance, how the cell density is responded and how one term can affect the other terms shown in the total flux vector $\underline{F}$ will be carefully examined.

Subject to the prescribed rotational flowfield and the initial conditions given as $n_o(t=0,\underline{x}) = 1000e^{-100[(x-0.25)^2+(y-0.25)^2]}$ and $c_0(t=0,\underline{x}) = 0$, the solutions computed at $\Delta t = 0.01\Delta x^2$ and $\Delta x = \Delta y = 0.01$ are plotted in Figs. 9–12 for the case investigated under $U_{max} = 0$ in $-0.5 \leqslant x, y \leqslant 0.5$. In Fig. 9(c), the center of the solution profile for n at $t = 0.0128$ is seen to move in the direction toward the corner because of the developing chemotaxic force. In Fig. 11, the chemotaxic force vector $\chi n\nabla c$ directs toward the rotation center while from Fig. 12 the diffusion force vector $D_n\nabla n$ is seen to be along the direction away from the rotation center. Both vectors have larger magnitudes near the rotation center. In view of Figs. 11(a) and 12(a), the effect of diffusion seems to dominate chemotaxis under the motionless condition.

To better understand the effect of convection, the values of U_{max} are increased from zero to $U_{max} = 1, 10$, and 100. The corresponding computed ratios of different flux terms are plotted in Figs. 13–17, respectively. The effects of the increased rotating flow velocity on the terms shown in the total flux vector $\underline{F}$ are summarized below:

1. Cell motion is caused by all the three forces in $\underline{F}$. The diffusion vector initially dominates the other two forces when the value of U_{max} is equal to 1.

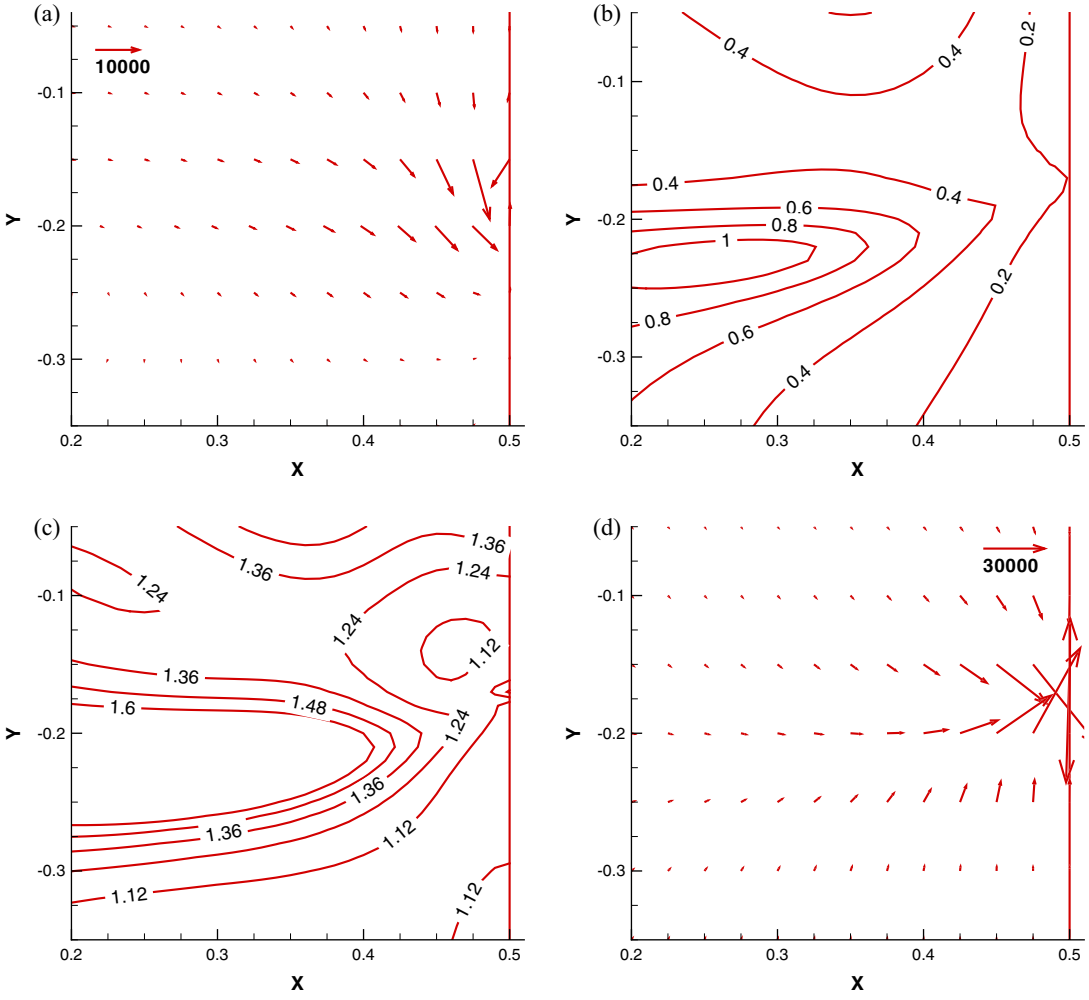

Fig. 21. The predicted ratios $\frac{|\mathbf{un}|}{|\nabla n|}$ and $\frac{|n\nabla c|}{|\nabla n|}$ at $t = 0.108$. The initial maximum velocity is 1. (a) total flux vector; (b) contours of the predicted ratio $\frac{|\mathbf{un}|}{|\nabla n|}$; (c) contours of the predicted ratio $\frac{|n\nabla c|}{|\nabla n|}$; and (d) the dominant vector in $\underline{F}$, which is the chemotaxic force vector.

2. At $U_{max} = 10$, convection force becomes dominant for all times. Diffusion also plays an important role near the boundary.
3. Chemotaxic force can make cells to aggregate near the zero-flux boundary for all the investigated values of U_{max} because of the accumulation of chemical attractant.
4. At the highest value of $U_{max}(= 100)$, blowup solution is never observed in this study. Higher convection prohibits the formation of high gradient chemical attractant (or ∇c). As a result, the solution for the cell density is bounded all the time.

5.3. Numerical study of the coupled NS–KS equations

We will finally solve the KS equations together with the Navier–Stokes equations in a domain containing an incompressible viscous fluid [19]. Solutions will be sought subject to the initial divergence-free velocity field $(u, v) = U_{max}(-cos\pi x\, sin\pi y, sin\pi x\, cos\pi y)$ in a truncated unit square $-0.5 \leqslant x, y \leqslant 0.5$. The computed time-evolving contours of n and the ratios of $\frac{|\underline{u}n|}{|\nabla n|}$ and $\frac{|n\nabla c|}{|\nabla n|}$ are plotted in Figs. 18–23, respectively. The blowup solutions generated by chemotaxic force are all computationally observable. A similar cell density distribution near or along the boundary is also observed because of the applied zero-flux boundary condition, thereby causing attractants to increase. Sometimes, convection plays an important role to result in blowup solution, because the inertial force has the same direction as the chemotaxic force. Two scenarios are observed in this study. In the beginning phase, cell density is driven either by convection or diffusion force. Chemotaxic force is not large enough in this stage, because chemical attractant is sparsely distributed in the locally low chemical concentration gradient flow. In the subsequent phase, chemotaxic phenomenon gradually becomes important because of the increasingly larger chemical concentration. Aggregation of the cell density starts at this moment and it is responsible for the subsequent blowup solution. In addition to the chemotaxic force, zero-flux boundary condition plays an essential role leading to the aggregation of the chemical attractant and cell density near the boundary, thereby finally resulting in the formation of blowup solution. Some conclusions are drawn below:

1. For the initial velocities under current investigation, the phenomenon governed by the KS–NS equations is controlled by flow convection in regions sufficiently apart from the boundary of physical domain. One can however observe the effect of chemotaxics, which is resulted from the high gradient chemical concentration, on the time evolving cell density in regions near the boundary.
2. While blowup solution is generated due to the formation of high-gradient chemical concentration in KS equations, this special phenomenon barely occurs in hydrodynamic system regardless of the initial mass of cell.

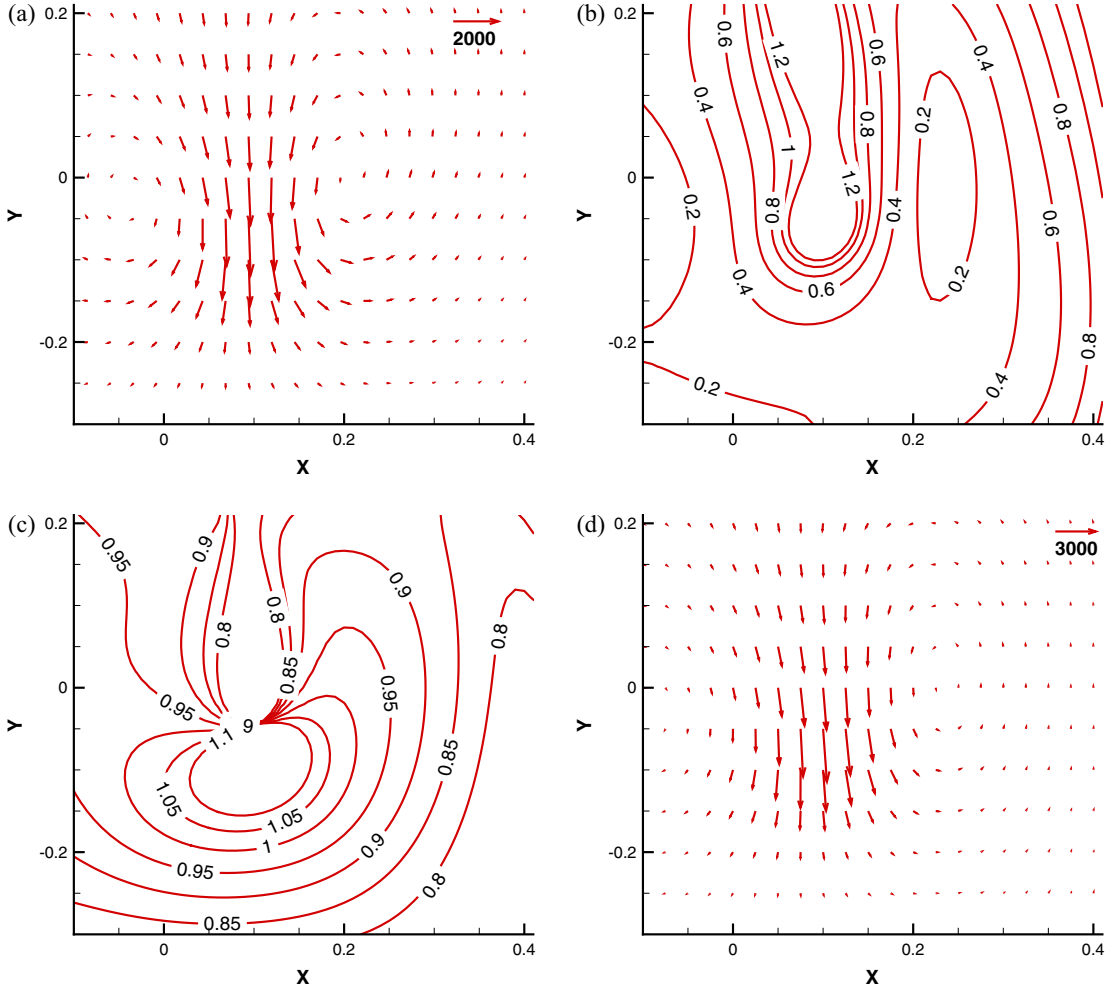

Fig. 22. The predicted ratios $\frac{|\underline{u}n|}{|\nabla n|}$ and $\frac{|n\nabla c|}{|\nabla n|}$ at $t = 0.1$. The initial maximum velocity is 10. (a) total flux vector; (b) contours of the predicted ratio $\frac{|\underline{u}n|}{|\nabla n|}$; (c) contours of the predicted ratio $\frac{|n\nabla c|}{|\nabla n|}$; and (d) the dominant vector in $\underline{F}$, which is the convection force vector.

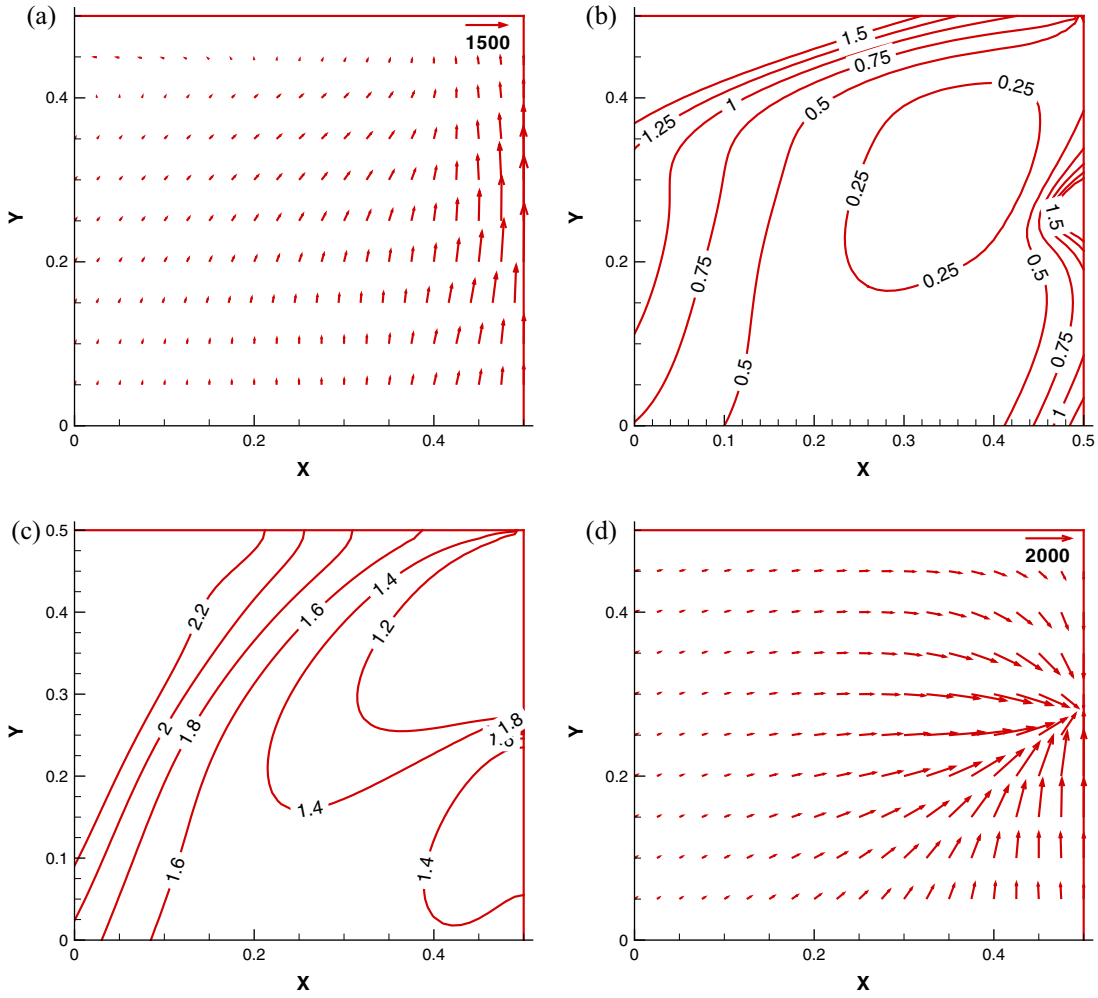

Fig. 23. The predicted ratios $\frac{|\mathbf{u}n|}{|\nabla n|}$ and $\frac{|n\nabla c|}{|\nabla n|}$ at $t = 0.32$. The initial maximum velocity is 10. (a) total flux vector; (b) contours of the predicted ratio $\frac{|\mathbf{u}n|}{|\nabla n|}$; (c) contours of the predicted ratio $\frac{|n\nabla c|}{|\nabla n|}$; and (d) the dominant vector in $\underline{F}$, which is the chemotaxic force vector.

6. Concluding remarks

The proposed combined compact difference scheme for approximating the Keller-Segel equations in a three-point grid stencil has been numerically verified for its application to the cases with/without considering the hydrodynamic equations. Several problems have been computationally studied in finite domain to revisit the analytically derived blow-up condition occurring in infinite domain. The effects of advection, diffusion and chemotaxis forces on the evolution of cell density are also addressed in this study.

References

[1] Keller EF, Segel LA. Model for chemotaxis. J Thero Biol 1971;30:225–34.
[2] Tuval I, Cisneros L, Dombrowski C, Wolgemuth CW, Kessler JO, Goldstein RE. Bacterial swimming and oxygen transport near contact lines. P Natl Acad Sci USA 2005;102:2227–82.
[3] Dolbeault J, Perthame B. Optimal critical mass in the two dimensional Keller-Segel model in $\mathbb{R}^2$. CR Acad Sci 2004;339:611–6.
[4] Herrero MA, Velazquez JJL. A blow-up mechanism for a chemotaxis model. Ann Scuola Norm Sci 1997;24:633–83.
[5] Lorz A. A coupled Keller-Segel-Stokes model: global existence for small initial data and blow-up delay. Commun Math Sci 2012;10:555–74.
[6] Chertock A, Kurganov A. A second-order positivity preserving central-upwind scheme for chemotaxis and haptotaxis models. Numer Math 2008;111:169–205.
[7] Patlak CS. Random walk with persistence and external bias. Bull Math Biophys 1953;15:311–38.
[8] Keller EF, Segel LA. Traveling bands of chemotactic bacteria: a theoretical analysis. J Theor Biol 1971;30:235–48.
[9] Filbet F, Laurencot P, Perthame B. Derivation of hyperbolic models for chemosensitive movement. J Theor Biol 2003;50:189–207.
[10] Filbet F. A finite volume scheme for the Patlak-Keller-Segel chemotaxis model. Numer Math 2006;104:457–88.
[11] Filbet F. Derivation of hyperbolic models for chemosensitive movement. J Math Biol 2003;50:189–207.
[12] Serini G, Ambrosi D, Giraudo E, Gamba A, Preziosi I, Bussolino F. Modeling the early stages of vascular network assembly. EMBO J 2003;22:1771–9.
[13] Tam CKW, Webb JC. Dispersion-relation-preserving finite difference schemes for computational acoustics. J Comput Phys 1993;107:262–81.
[14] Sheu TWH, Hung YW, Tsai MH, Chiu PH, Li JH. On the development of a triple-preserving Maxwell's equations solver in non-staggered grids. Int J Numer Meth Fluids 2010;63:1328–46.
[15] Sheu TWH, Chiu PH. A divergence-free-condition compensated method for incompressible Navier–Stokes equations. Comput Method Appl M 2007;196:4479–94.
[16] Epshteyn Y, Izmirlioglu A. Fully discrete analysis of a discontinuous finite element method for the Keller-Segel chemotaxis model. SIAM J Sci Comput 2009;40:211–56.
[17] Blanchet A, Dolbeault J, Perthame B. Two-dimensional Keller-Segel model: optimal critical and qualitative properties of the solutions. EJDE 2006;44:1–32.
[18] Fatkullin I. A study of blow-ups in the Keller-Segel model of chemotaxis. Preprint, arXiv:1006.4978, 2011.
[19] Chertock A, Fellner K, Kurganov A, Lorz A, Markowich PA. Sinking, merging and stationary plumes in a coupled chemotaxis-fluid model: a high-resolution numerical approach. J Fluid Mech 2012;694:155–90.